

LAMINAR SEPARATION CONTROL EFFECTS OF SHORTFIN MAKO SHARK SKIN

by

MICHAEL THOMAS BRADSHAW

AMY W. LANG, COMMITTEE CHAIR  
SEMIH M. OLCMEN  
PHILIP J. MOTTA

A THESIS

Submitted in partial fulfillment of the requirements  
for the degree of Master of Science  
in the Department of Aerospace Engineering and Mechanics  
in the Graduate School of  
The University of Alabama

TUSCALOOSA, ALABAMA

2014

Copyright Michael Thomas Bradshaw 2014

**ALL RIGHTS RESERVED**

## ABSTRACT

Shark skin is investigated as a means of laminar flow separation control due to its preferential flow direction as well as the potential for scales to erect and obstruct low-momentum backflow resulting from an adverse pressure gradient acting on the boundary layer. In this study, the effect of the scales on flow reversal is observed in laminar flow conditions. This is achieved by comparing the flow over a pectoral fin from a shortfin mako shark to that over the same fin that is painted to neutralize the effect of the scales on the flow. The effect of the scales on flow reversal is also observed by comparing the flow over a smooth PVC cylinder to that over the same cylinder with samples of mako shark skin affixed to the entire circumference of the cylinder. These samples were taken from the flank region of the shark because the scales at this location have been shown to have the greatest angle of erection compared to the scales on the rest of the shark's body. Scales at this location have an average crown length of 220  $\mu\text{m}$  with a maximum bristling angle of proximately 50 degrees. Because these scales have the highest bristling angle, they have the best potential for separation control. All data was taken using time-resolved Digital Particle Image Velocimetry. The flow over the pectoral fin was analyzed at multiple angles of attack. It was found that the shark skin had the effect of decreasing the size of the separated region over both the pectoral fin and the cylinder as well as decreasing the magnitudes of the reversing flow found in these regions. For all Reynolds numbers tested, drag reduction over 28% was found when applying the sharkskin to the cylinder.

## NOMENCLATURE

$\alpha$	Pectoral fin angle of attack
$c$	Pectoral fin chord length
$D$	Diameter of cylinder
$Re$	Reynolds number based on chord length or diameter
$U$	Free stream velocity
$u$	Mean velocity in the tangential direction of the local flow
$v$	Mean velocity in the normal direction of the local flow

## ACKNOWLEDGMENTS

I would like to thank my advisor and committee chair, Dr. Amy Lang, for making this research possible and allowing me to work under her guidance for the past several years. I also thank Dr. Semih Olcmen and Dr. Philip Motta for serving on my thesis committee and offering their advice and expertise. Much thanks also goes to Dr. Philip Motta and Laura Habegger of the University of South Florida, as well as Robert Heuter of Mote Marine Laboratory, for their biological expertise as well as the procurement and preparation of the skin samples. I am very grateful for the guidance and help from students in the water tunnel lab: Drew Smith, Nikki Wheelus, Emily Jones, and Mark Koren. Much of this work could also not have been completed without the hard work and guidance from the engineering machine shop workers at the University of Alabama. They are responsible for the construction of the model mounting brackets. I also greatly appreciate the support from the University of Alabama Graduate Council as well as the National Science Foundation grant #1062611 (to Amy Lang) that has allowed me to continue to pursue my education and fund this research. Finally, I would like to thank my wife, Julia, for all of her support and patience during the past year.

## TABLE OF CONTENTS

ABSTRACT.....	ii
NOMENCLATURE.....	iii
ACKNOWLEDGEMENTS.....	iv
LIST OF TABLES.....	viii
LIST OF FIGURES.....	ix
1. INTRODUCTION.....	1
1.1 LAMINAR BOUNDARY LAYER SEPARATION.....	1
1.2 SHARK SKIN SEPARATION CONTROL TECHNIQUES.....	2
1.3 OBJECTIVE.....	6
2. REVIEW OF LITERATURE.....	9
2.1 LAMINAR BOUNDARY LAYER SEPARATION.....	9
2.2 SEPARATION CONTROL TECHNIQUES.....	11
2.3 SHARK SKIN FLOW CONTROL.....	14
3. EXPERIMENTAL CONFIGURATION.....	18

3.1 EXPERIMENTAL FACILITY.....	18
3.2 DPIV SYSTEM.....	19
3.3 EXPERIMENTAL MODELS.....	24
3.4 EXPERIMENTAL PROCEDURE.....	28
4. RESULTS AND DISCUSSION.....	32
4.1 SHORTFIN MAKO PECTORAL FIN.....	32
4.1.1 BACKFLOW COEFFICIENT.....	33
4.1.2 AVERAGE BACKFLOW MAGNITUDE.....	37
4.2 CYLINDER.....	41
4.2.1 BACKFLOW COEFFICIENT.....	42
4.2.2 AVERAGE BACKFLOW MAGNITUDE.....	46
4.2.3 VELOCITY HISTORY.....	50
4.2.4 MOMENTUM ANALYSIS.....	52
5. CONCLUSIONS.....	55
5.1 SHARK SKIN SEPARATION CONTROL.....	55

5.2 ECOLOGICAL IMPLICATIONS FOR THE SHORTFIN MAKO.....	57
5.3 FUTURE WORK.....	57
REFERENCES.....	59
APPENDIX-UNCERTAINTY ANALYSIS.....	62

## LIST OF TABLES

1. Length scale calibration and field of view of processed images.....	31
2. Results of summing velocity over left and right boundaries.....	54
3. Percent drag reduction when shark skin is applied to cylinder.....	54

## LIST OF FIGURES

1. View of laminar separation, transition, and reattachment (Horton, 1967).....	2
2. SEM profile view of Shortfin Mako scales (Lang, 2011).....	4
3. Diagram of scale maximum bristling angles by location (Motta et al., 2012).....	6
4. Boundary layer near the point of separation (from Schlichting, 1979).....	10
5. SEM of individual shark scale to show base dimensions (Lang et al. 2011).....	17
6. Water tunnel calibration curve.....	19
7. Quantronix Falcon 30 series Nd:YLF laser.....	20
8. Quantronix Darwin-527-M laser head.....	21
9. Basler A504k 8-bit high-speed camera with Nikon AF Micro Nikkor 105mm lens.....	22
10. Top-down diagram of experimental setup in water tunnel test section.....	23
11. Left pectoral fin attached to mounting bracket.....	25
12. Angle of attack dial for pectoral fin mounting bracket.....	25
13. Cylinder and mounting bracket in water tunnel test section.....	26

14. Smooth PVC cylinder and PVC cylinder with attached shark skin.....	27
15. Measurement locations for pectoral fin (left) and cylinder (right).....	29
16. Backflow coefficient contours, $Re=86,000$ , $\alpha=4^\circ$ .....	34
17. Backflow coefficient contours, $Re=55,000$ , $\alpha=4^\circ$ .....	34
18. Backflow coefficient contours, $Re=55,000$ , $\alpha=8^\circ$ .....	35
19. Backflow coefficient contours, $Re=55,000$ , $\alpha=12^\circ$ .....	36
20. Backflow coefficient contours, $Re=86,000$ , $\alpha=12^\circ$ .....	37
21. Average backflow magnitude contours (m/s), $Re=55,000$ , $\alpha=8^\circ$ .....	38
22. Peak backflow magnitude, $Re=55,000$ , $\alpha=8^\circ$ .....	38
23. Average backflow magnitude contours (m/s), $Re=55,000$ , $\alpha=12^\circ$ .....	39
24. Peak backflow magnitude, $Re=55,000$ , $\alpha=12^\circ$ .....	39
25. Average backflow magnitude contours (m/s), $Re=86,000$ , $\alpha=12^\circ$ .....	41
26. Peak backflow magnitude, $Re=86,000$ , $\alpha=12^\circ$ .....	41
27. Backflow coefficient contours, $Re=22,400$ .....	43
28. Polar backflow coefficient contours, $Re=22,400$ .....	44

29. Polar backflow coefficient contours, $Re=29,400$ .....	45
30. Polar backflow coefficient contours, $Re=45,000$ .....	46
31. Average backflow magnitude, $Re=22,400$ .....	48
32. Average backflow magnitude, $Re=29,400$ .....	49
33. Average backflow magnitude, $Re=45,000$ .....	50
34. Instantaneous velocity data.....	51
35. Time averaged velocity fields.....	52
36. Velocity profile used in drag calculation.....	53

## 1. INTRODUCTION

### 1.1 LAMINAR BOUNDARY LAYER SEPARATION

Flow over an object has the tendency to separate when it encounters an adverse pressure gradient. The adverse pressure gradient must be of sufficient strength to stop or reverse the fluid flowing in the boundary layer. This adverse pressure gradient can be due to either the shape of the object or its orientation in the flow. Once the flow is separated, the flow behind the separation point typically comprises a vortex filled wake such that it differs drastically from the predictions of inviscid theory. This has the effect of significantly increasing the pressure drag on the object (Schlichting, 1979). One such example of the effect of flow separation over an object can be seen in the lift curve of an airfoil. As the airfoil increases in angle of attack, the lift produced by the airfoil continues to increase until reaching the stall angle. At the stall angle, the adverse pressure gradient is large enough to create a region of separated flow over the airfoil and the lift produced begins to decrease with the increasing angle of attack.

In a laminar boundary layer, flow separation begins at a point on the surface where the adverse pressure gradient has resulted in zero shear stress at the wall causing the reversal of flow in the region above the wall. Past the point of separation, the positive-direction flow is detached from the surface until the point of reattachment, resulting in a separation bubble. In the separated region, the flow transitions to turbulent, and will reattach to the surface.

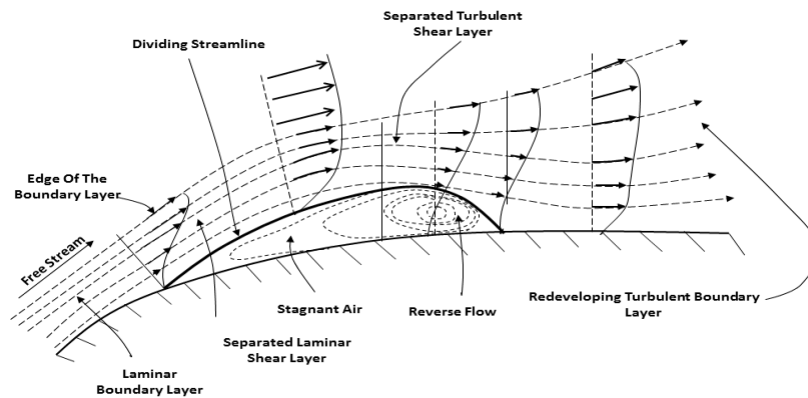


Figure 1.1: View of laminar separation, transition, and reattachment (Horton, 1967)

## 1.2 SHARK SKIN SEPARATION CONTROL TECHNIQUES

Flow control found in nature has been an area of interest in the field of fluid mechanics and flight for many years. Man received the inspiration and desire to fly by observing animals that naturally possess such abilities. In nature, the wings of birds and insects, as well as the skin of fish and other marine animals differ greatly from those surfaces used on civil and military aircraft. While these natural aerodynamic surfaces have existed for millions of years in nature, relatively little quantitative research has been done to determine the possible benefits of using these surface patterns on modern aerospace technology. Through the use of visual flow measurement techniques, such as digital particle image velocimetry, it has become possible to analyze flow over such micro-patterned surfaces.

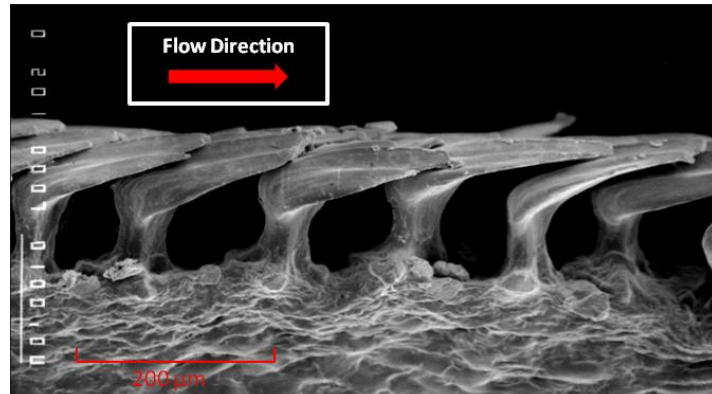
One particular animal of interest is the Shortfin Mako shark (*Isurus oxyrinchus*). The Shortfin Mako was chosen as the focus of this research because it is considered to be one of the fastest and most agile of pelagic (oceanic) sharks (Stevens, 2009). The shark has been observed to maintain high speeds while bursts of speeds of over 20 meters per second have been recorded

(Videler, 1995). The average speed that has been observed for the Shortfin Mako is ten body lengths per second. Observation of the animal in its natural habitat has shown the shark to be extremely agile and maneuverable, able to make sudden changes in direction at very high speeds and also in rapid succession. The Shortfin Mako is also one of the more derived species of shark. Its origins have been traced back to approximately 55 million years ago in the line of shark evolution dating back more than 400 million years (Naylor et al., 1997).

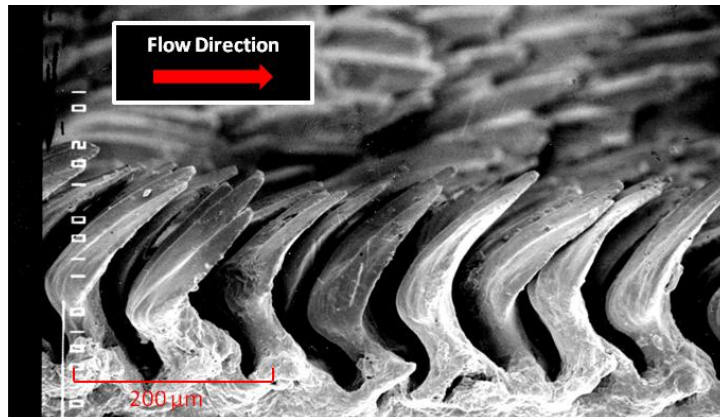
The Shortfin Mako can be found around the globe in warm-temperate and tropical seas and is typically found in offshore waters. The Shortfin Mako is estimated to have a maximum length of 408 cm (~13.4 feet). Males have been recorded to reach a length of 298 cm while the females have been recorded to exceed 390 cm (Compagno, 1984). Shortfin Makos are thunniform swimmers meaning that only the tail and caudal peduncle undulate to produce swimming motion (Maia et al., 2012). While the primary source of food for the Shortfin Mako includes teleosts, many fast fish such as mackerels, tuna, swordfish, and other sharks are also prey (Maia et al., 2006). The Shortfin Mako also has very few predators, which could be attributed to its speed and high level of activity (Compagno, 1984). The streamlined shape of the Shortfin Mako shark's body is believed to contribute to drag reduction and it has also been suggested that the placoid scales covering the shark's body also play an important role in drag reduction and flow separation control (Bechert, 2000).

These scales, also known as dermal denticles, average 0.2 mm in length from at any given location on the shark's body. They are oriented in rows from the head to tail of the shark (Reif, 1985a). They have a similar morphology to human teeth, with a hard outer enameloid layer encasing a softer dentine core. This property, as well as the ratio of base length to width allows the scales to pivot about their base when bristled manually (Motta et al., 2012). Scanning

electron microscope (SEM) images by Lang show the three-dimensional geometry of each scale. It can also be seen that the tips of the scales overlap the base of the next row of scales (Figure 1.2(a)) Figure 1.2(b) shows an SEM image of the scale when they are manually bristled in a laboratory setting.



(a)



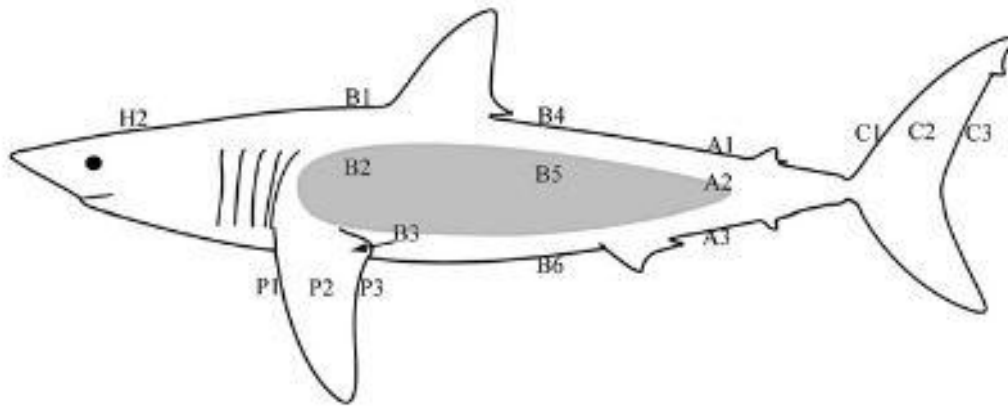
(b)

Figure 1.2(a) SEM profile view of non-bristled Shortfin Mako scales. (b) SEM profile view of manually bristled and dried Shortfin Mako scales (Lang, 2011).

Previous research at the University of Alabama has proven that when an isolated skin sample was subjected to a reversed flow, opposite of the preferred flow direction, the scales do in fact bristle when they encounter a reversed flow, opposite of the preferred flow direction indicated in Figure 1. Such a reversed flow can be encountered under separated boundary layer conditions (Schlichting, 1979). It is theorized that under this reversed flow when the scales are

bristled, vortices are generated within the cavities that are present between the erected scales. The vortices then cause a partial slip condition to occur over the tops of the bristled scales which helps to impede the separation of the boundary layer (Lang et al., 2011). Local separation, such as what is hypothesized by in this work, would have a great benefit for the shark in impeding separation over the body of the shark, and therefore, reducing the pressure drag that would be encountered by this animal. The scales can be thought of as providing a “dynamic roughness” to the surface of the shark (Lang et al. 2014).

It has also been shown in work by Lang et al. (2011) and more recently by Motta et al. (2012) that the individual scales can be manually bristled up to a maximum angle. Figure 1.3 shows the varying degree of maximum bristling angle that can be found over the body of the Shortfin Mako shark. Over the shark, in concordance with the varying angle of attack that the scales can reach, the ratio of base length to width of the scales also varies. At the location where the maximum base length to width ratio was measured (flank region), the maximum angle of attack is observed (Motta et al., 2012). It can be seen from this diagram this location of maximum bristling angle occurs in the flank region of the shark. The flank region is aft of the widest portion of the shark, which is also a location where separation is likely to occur. A higher degree of bristling at this location further supports the hypothesis that the scales act to inhibit separation over the shark. Because the scales with higher bristling angles have the greatest potential to reach higher into the boundary layer to control the separation, skin samples from the flank region are used in this experiment. According to Lang et al. (2011), when erected, the scales extend to approximately 2% of the boundary layer.



Location	Angle (deg.)	Location	Angle (deg.)
H2	33±1	A2	39±1
B1	28±1	A3	16±3
B2	48±1	P1	1±1
B3	30±1	P2	23±1
B4	25±1	P3	32±2
B5	43±2	C1	25±2
B6	28±1	C2	28±1
A1	25±1	C3	30±2

Figure 1.3 Diagram of scale maximum bristling angles by location (Motta et al., 2012)

### 1.3 OBJECTIVE

The objective of this research was to compare the separation and flow characteristics over surfaces with applied shark skin to the same surfaces with no shark skin under laminar conditions. Such a comparison allows for the evaluation of the separation control effectiveness. The two objects of interest in this research were a pectoral fin, with a span of approximately 71 cm, from an adult Shortfin Mako and a cylinder with a diameter of 8 cm. The flow over both surfaces was analyzed primarily using a time-resolved digital particle image velocimetry (TR-

DPIV) system. The experiments were performed in the water tunnel facility at the University of Alabama. This system is further explained in the Experimental Configuration section.

The use of the pectoral fin allows for the shark skin to be analyzed under its natural application. The pectoral fin used has a length from root to tip of 71 cm (28 inches) and an average chord length of 15.25 cm (6 inches). In nature, this fin would approach Reynolds numbers of 3,000,000 based on the average chord length of 15.25 cm. While the water tunnel facility at the University of Alabama is only capable of subjecting the fin to a Reynolds number of 86,000 based on the average chord length, analyzing the fin at low Reynolds numbers will offer insight into the mechanics of the scales and separation control under laminar conditions. The fin also has camber, which will create an adverse pressure gradient and result in flow separation at high enough angles of attack. The flow over the fin was first analyzed using just the natural fin. The specimen was frozen until experimentation. Before beginning the experimentation, it was allowed to thaw. It was then sprayed with Elmer's spray adhesive and painted with Rustoleum latex based paint to neutralize any effect the scales may have on the characteristics of the flow. The same tests were conducted again for the painted fin as a control case. For both cases, the fin was run at various angles of attack, ranging from 0 degrees to 12 degrees, where similar shaped airfoils would experience stall conditions, meaning the flow is completely detached from the surface. The free stream speed of the water tunnel was also varied for this experiment.

The cylinder was tested using a similar method to evaluate the effectiveness over a surface where flow separation is inevitable. The curvature of the cylinder induces an adverse pressure gradient, which is necessary for creating flow separation. The smooth PVC cylinder was first analyzed under different water tunnel free stream speeds. Then shark skin with was applied

around the circumference of the cylinder, the flow was then analyzed over the shark skin surface, and the two surfaces were compared. For both the pectoral fin and the cylinder, the flow was evaluated primarily by the backflow coefficient. The backflow coefficient is defined as the percentage of time that flow is reversed, with respect to the total time elapsed for each set of data. This parameter is a good indication of the location and size of the separated region (Smith, 2011). Average backflow magnitude was also analyzed in order to evaluate the amount of momentum contained in the separated region. Velocity and other data were also used to compare the flow over the different surfaces. A momentum analysis was performed to obtain drag measurements over the cylinder comparing the plain cylinder to the cylinder with applied shark skin.

## 2. REVIEW OF LITERATURE

### 2.1 LAMINAR BOUNDARY LAYER SEPARATION

Laminar boundary layers have been the source of much investigation over the last century. The boundary layer is formed as the velocity increases rapidly from the zero velocity, no-slip condition at the surface to the value of the free stream velocity due to the presence of shear stress in the flow. In this way, real fluids differ from ideal fluids because they have an inherent viscosity. Along a surface or a body, the thickness of the boundary layer begins to grow until this boundary layer becomes separated under an adverse pressure gradient (Schlichting, 1979).

One example commonly used to explain the phenomenon of boundary layer separation is the flow past a cylinder. When a particle in the flow is moving from the leading edge to the point of maximum thickness over a cylinder, particle velocity is increased due to the transfer of energy from pressure to kinetic energy. After it reaches the point of maximum thickness and moves toward the trailing edge, the kinetic energy is transformed again into pressure but in the opposite direction of the flow. This gives rise to an adverse pressure gradient due to the point of minimum pressure now being located upstream and thus the boundary layer is prone to separation (Schlichting, 1979). Because the flow in the boundary layer has very low momentum, a small adverse pressure gradient can greatly affect the flow characteristics. The low momentum fluid tends to be reversed and flows in a direction that is opposite to that of the free stream flow. This irregularity in the flow results in the flow detaching from the object and the formation of a

low pressure wake and high pressure drag over the body. Over an object such as an airfoil, such flow separation can lead to loss of lift, as evidenced by the peak and drop of the lift coefficient of a typical airfoil lift curve. Figure 2.1 shows boundary layer flow close to the point of separation (Schlichting, 1979). It can be seen that as the adverse pressure gradient begins to reverse the low momentum fluid in the boundary layer, an area of separated flow begins to form.

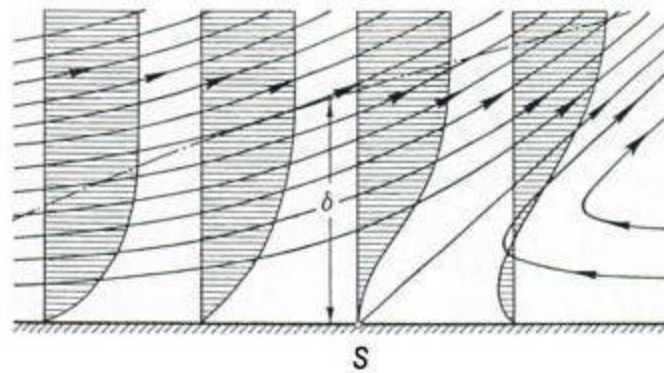


Figure 2.1 Boundary layer near the point of separation (from Schlichting, 1979)

Laminar flow over airfoils has been widely studied. Over an airfoil, flow has been observed to detach. When the flow reattaches, the detached flow is said to be in a bubble. Tani (1964) found that when a flow separated over the surface of an airfoil, the pressure drag benefits of having attached flow are lost. However, it was found that if the flow in the separated region transitioned to turbulent and then reattached, some of the dynamic pressure loss could be recovered, which is generally favorable.

In a study of the boundary layer over an elliptical cylinder (Schubauer, 1936) compared the numerical solution of the laminar boundary layer to that obtained experimentally. Using a hotwire anemometer, it was found that after the point of separation, the validity of previously derived laminar boundary layer equations was diminished. After the flow reaches a point close to

the maximum thickness of the cylinder, it begins to detach, and the flow characteristics were not predicted by laminar boundary layer theory. Because separation over a cylinder is inevitable due to the adverse pressure gradient created by the shape of the body, the cylinder was chosen to be one surface evaluated in this study.

## 2.2 SEPARATION CONTROL TECHNIQUES

Flow separation control techniques can be classified as either passive or active. Active separation control techniques are defined as methods that require an external energy input to eliminate or delay boundary layer separation. While these techniques can be effective, they are undesirable because of the energy requirement. Several active separation control techniques have been investigated and proved to be effective. One such technique was investigated by Andino (2005). In this study, the effect of zero-net mass actuators on the separation of boundary layers using a NACA 4412 airfoil was investigated. An adverse pressure gradient was induced by increasing the angle of attack of the airfoil. Acting as artificial jets, the actuators pull low momentum fluid in from the boundary layer, and then eject the same fluid back in to the boundary layer with a higher momentum. By varying the frequency of the actuators, as well as the volume capacity, it was found that the actuators were able to restore attachment of a fully separated flow with higher rates of actuation and were able to eliminate periodic separation with low frequency actuation.

Passive separation control mechanisms and techniques have been the subject of much investigation. One means of achieving passive flow control is to alter the surface geometry over which the fluid passes. Passive separation control techniques are highly desirable over active techniques because they do not require an input of additional energy to be activated or actuated:

they rely on the energy present in the flow. One very common method of passive flow separation control is the use of vortex generators. Vortex generators are small, vertical protrusions into the boundary layer that can be used on the surface of an aerodynamic object, such as on the surface of a wing. The vortex generators are typically arranged in v-shaped formations along a single spanwise line on a wing. The location and size of the vortex generators depends highly on the nature of the flow over the surface. As flow encounters these vortex generators, vortices with axes aligned in the streamwise direction are created downstream which help to increase momentum of the fluid within the boundary layer in the near vicinity of the surface and thus make this region of flow less prone to reversal.

Lin (2002) investigated the effectiveness of low profile vortex generators over an airfoil. These vortex generators had a height varying from 10% to 50% of the boundary layer thickness. It was found that the vortex generators induced high momentum flow into the lower region of the boundary layer, which was present in the flow even beyond the dissipation of the vortices. Such increase in momentum was found to increase lift over various airfoils at both low and high Reynolds number. This increase of momentum helps to overcome the separation present in an adverse pressure gradient. However, such vortex generators can cause an increase in skin friction drag. In addition to the separation control aspect, these generators were found to be beneficial in other areas, such as the reduction of interior aircraft noise (Lin, 2002). The hydrodynamic performance of vortex generators was evaluated by Brandner et al. (2002). The flow geometry over a delta shaped vortex generator was modified by cavitation in the testing facility. In the many different geometric flow conditions, it was found that the mixing induced by the vortex generator remains an effective way to maintain a favorable lift to drag ratio.

Another means of passive flow separation control is the use of self-activated moveable flaps which was investigated Bechert et al. (2000). Flight tests were performed on an aircraft having laminar flow over the wings with moveable flaps present near (85-95% of chord) the trailing edge. The flaps are freely hinged to allow for self-activation. Under attached flow conditions, the flaps remained inactive. However, when the flow was detached, the flaps were passively activated by the backflow. It was found that the use of the flaps allows for a 3.5% reduction in the minimum attainable speed before stall due to delayed flow separation. These results were also obtained in wind tunnel testing. The use of passively activated flaps was also investigated by Schatz et al. (2004). The flaps, which closely resemble the outer layer of feather on the upper surface of bird wings, were experimentally and numerically investigated when employed on airfoils. It was found that such flaps increased lift by more than 10%. Lift is increased by means of flow separation control. The flap acts to block the reversed flow found in a separated boundary layer. Such a blockage results in a delayed flow separation over the airfoil.

Transverse grooves were proposed as a means of separation control and drag reduction by Bushnell (1983). It was theorized that the grooves give rise to embedded vortices trapped in each groove. The vortices cause a partial slip condition to develop over the tops of the grooves. This partial slip condition allows for less shear to be encountered than when a no-slip condition is present at the wall. The partial slip condition also decreases the momentum loss in the boundary layer, which can help to delay the onset of flow separation. Howard (1985) also studied the effect of transverse grooves on separation control and drag characteristics. Using axisymmetric bluff bodies, he made grooves around the circumference of the bodies. When comparing the grooved bodies to their smooth counterparts, he found that the grooves delayed

the onset of a separated boundary layer, and restricted the separated areas to smaller regions. This also resulted in a decrease in overall drag.

Flow control over a NACA 0012 airfoil with applied V-shaped micro-riblet film was investigated by Lee and Jang (2005). The height of each groove was  $176.8 \mu\text{m}$  and the spacing between each groove was  $300 \mu\text{m}$ . It was found that at Reynolds number of 46,000, the riblets acting as surface roughness interacted with the streamwise vortices, leading to an increase in the size of the vortex formation region and the wake width when compared to the smooth airfoil. The drag coefficient was also increased with the application of the micro-riblets. At a low Reynolds number (15,000), drag is reduced, and the grooves reduce the vortex formation lengths.

Similarly, flow control over a circular cylinder was also investigated using V-grooved micro riblets (Lee et al., 2005). The size and spacing of the riblets were the same as in the previous experiment over the NACA 0012 airfoil. Comparing a smooth cylinder to a cylinder with V-grooved micro-riblet film attached, differences were noticed in the drag measurements as well as the characteristics of the wake. Over the smooth surface, the region of vortex formation was found to be  $x/D=3.8$  while this value was equal to 3.4 for the grooved surface. At low Reynolds numbers (under  $10^4$ ), the riblets decreased the measured drag coefficient, while above this Reynolds number, the drag coefficient was increased.

### 2.3 SHARK SKIN FLOW CONTROL

Biological surfaces have been increasingly studied over the years as a way to improve current and future technology. In the field of fluid dynamics, shark skin has been looked to as a possible means of drag reduction and separation control. Initial investigations of the flow control mechanisms of shark skin focused primarily on the grooves on the scale surfaces, which act as

riblets, or grooves along the flow direction, in the flow. Bruse (2000) found that these grooves on the surfaces of the scales help to reduce drag by inhibiting cross flow, or flow perpendicular to the free stream direction, which can decrease the skin friction drag for a turbulent boundary layer by about 8-9%. While this research did result in some drag reduction, these studies gave no consideration to the possible bristling aspect of the scales.

Bechert et al. (2000) measured the shear stress present over a flat plate shark skin model in a turbulent oil tunnel. The scales were fixed to a compliant anchor system consisting of springs of various tensions to allow for some actuation from the flow. The scales were also able to be set to a specific angle of attack. When the scales were laid flat on the surface, it was observed that the shear stress, and therefore skin friction drag, was decreased by approximately 3% when compared to a smooth plate. Using the soft compliant anchor, the scales were observed to have varying behaviors. When the turbulence of the experiment was low, the scales were observed to move to the position lying flat on the surface. However, when the local turbulence is high, the individual scales pivot in response to the locally varying instantaneous flow conditions within the boundary layer. When the scales were fixed at various angles with a somewhat rigid anchor, it was found that the skin friction drag over the scales actually increased.

More recent work performed by Lang and Hidalgo (2009) also focused on flow over erected shark scales. A shark skin model of 100:1 scale was created by use of rapid prototyping techniques. This scale was chosen in order to have Reynolds number similarity. When the scales in this model were fixed to a 90 degree angle of attack, which was suspected to be an example of extreme bristling, vortices were observed to form in the cavities between the scales. This extreme bristling angle has since been refuted by Motta et al. (2012). The average velocity over the top of the scales was recorded to be approximately 14% of the free stream velocity. Such a

measurement indicates that the embedded vortices between the scales induce a partial slip condition, compared to a no-slip condition that would be present over a flat surface. It was also noted that a greater degree of mixing between the low momentum fluid in the cavities and the high momentum fluid higher in the boundary layer was occurring. It was also theorized that shark skin can help mitigate flow separation.

Motta et al. (2012) conducted tests on the scales of several species of sharks to verify the degree of bristling that occurs for the scales. The species that were included in this study were the great hammerhead (*Sphyrna mokarra*), the blacktip (*Carcharhinus limbatus*), and the Shortfin Mako (*Isurus oxyrinchus*). To bristle the scales, a pressure cuff was placed under the skin and pressurized to 15 psi. Bristling was not observed by altering the pressure under the scales leading to the hypothesis that the scales may be bristled passively. On the samples from the hammerhead and the blacktip, the scales could be manually bristled by a fine acupuncture needle to a resting angle slightly greater than 30 degrees. However, on the Shortfin Mako, the maximum bristling angle of flank scales was approximately 50 degrees. Because of the great speed of the Shortfin Mako, as well as the possible bristling of the shark's scales, it was theorized that the scales on the surface of the shark might aid in delaying flow separation during rapid swimming. It was also found that the location of the shark with the highest degree of bristling is the flank region, which is located aft of the point of maximum body thickness of the shark. Because this is likely where flow separation will occur and the degree of bristling is very high at this location, skin samples from this region were chosen for further tests. When viewed under SEM, the base length and width of the scales were seen to vary widely over the shark. The ratio of base length to width corresponds to the scale flexibility, as the scales with the highest

degree of bristling were found to have the smallest base length to width ratio. Figure 2.2 shows the base of a sample denticle.

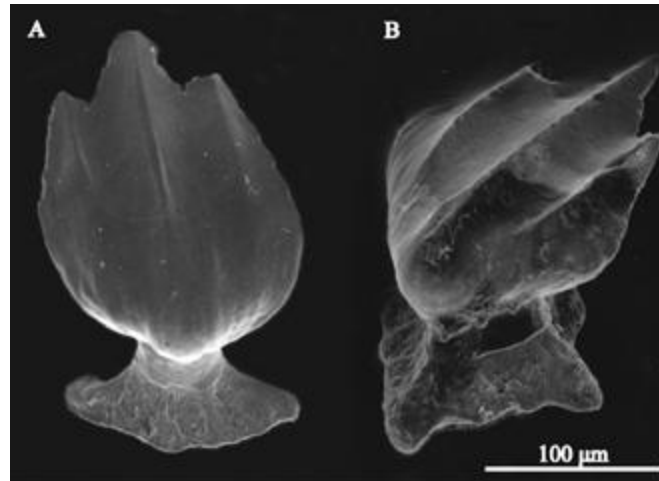


Figure 2.2 SEM of individual shark scale to show base dimensions (Lang et al. 2011).

Work performed by Smith (2011) analyzed the effectiveness of the shark skin in controlling flow separation over a NACA 4412 hydrofoil in tripped turbulent conditions. It was theorized in this research that in order for the scales to bristle, a sufficient shear must be present in the flow. Results agreed with this hypothesis, as the shark skin was not effective in controlling the size of the separated region and the point of separation until the angle of attack was beyond 12 degrees. At high angles of attack, it was found that the distance from the trailing edge to the point of detachment was decreased by up to 27% when the shark skin was employed. It was concluded that the bristling and impedance of the flow reversal is the source of the separation control.

### 3. EXPERIMENTAL CONFIGURATION

#### 3.1 EXPERIMENTAL FACILITY

All experiments for this research were conducted in the water tunnel facility at the Department of Aerospace Engineering, University of Alabama. The water tunnel is a modified Eidetics Model 1520 water tunnel manufactured by Rolling Hills Research Corporation in El Segundo, California. The standard model has a volume capacity of approximately 1000 gallons and a test section length of 60 inches. The modified water tunnel (1520 EXT) has an extended test section compared to the standard model. The test section has a length of 108 inches and a height of 30 inches. Because the test section is extended, the width of the test section expands from 16.25 inches at the inlet to 17.25 inches at the outlet to account for the boundary layer growth along the walls of the test section. With the use of a high speed impeller, the tunnel is capable of sustaining free stream speeds exceeding 1.64 ft/s (0.5 m/s) in the test section. The impeller is driven by a 2.0 horsepower, 230 V, 3-phase electric motor with 0-60 Hz rotation frequency range. The water tunnel speed calibration curve for the frequency of the motor is shown in Figure 3.1. The calibration was performed soon after the installation of the water tunnel by use of DPIV to calculate the water speeds. This curve is used to approximate the free stream speed during tests. Although the temperature in the water tunnel may vary slightly, it is estimated that the density and the viscosity in the water tunnel stay relatively constant. For all calculations, a density of  $1000 \text{ kg/m}^3$  and viscosity of  $.00089 \text{ kg/m}\cdot\text{s}$  are used.

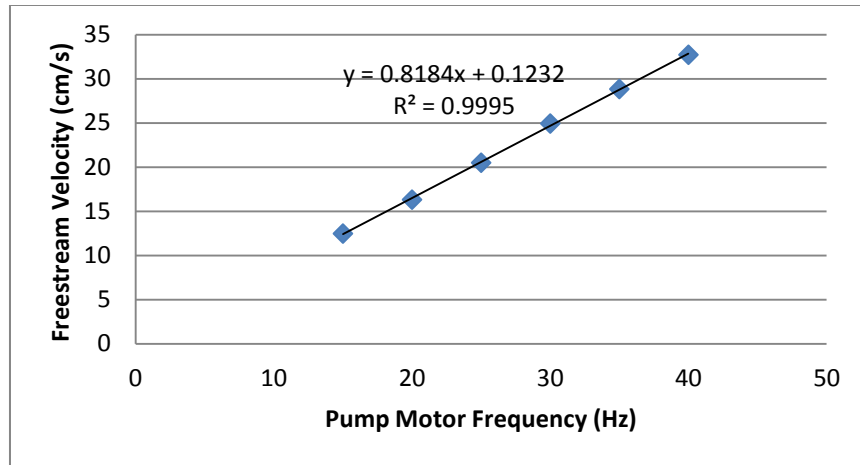


Figure 3.1 Water tunnel calibration curve

In addition to the test section modification, the water tunnel has two additional stainless steel baffles within the inlet chamber that help to improve flow distribution and reduce free-stream turbulence. To further reduce the turbulence, two porous plates and three stainless steel screens are present along with the honeycomb structure between the inlet plenum and the test section. This ensures the flow entering the test section is uniform. Tests conducted by the manufacturer show that the modifications present in the water tunnel result in an average turbulence intensity of 0.41% at a test section free stream velocity of 2.0 in/s. The water tunnel must be regularly cleaned and flushed of water in order to minimize the effect of particle fouling on the screens or the honeycomb. Pressurized water is the primary means of cleaning the surfaces in the tunnel.

### 3.2 DPIV SYSTEM

All data for this research was obtained using a two-dimensional time-resolved digital particle image velocimetry system. The system consists of a pulsed solid-state laser, an optical array for the manipulation of the laser beam, a high speed digital camera, image acquisition

software, and DPIV processing software. Particles are used to seed the water in order for the fluid motion to be tracked. The particles used are Potters Industries, Inc. silver coated glass spheres with an average diameter of 14  $\mu\text{m}$ . The particles are neutrally buoyant in water in order to closely follow the motion of the water.

A Falcon 30 series Nd:YLF laser manufactured by Quantronix Corporation was utilized (Figure 3.2). This laser generates a beam with a wavelength of 532 nm and a maximum power output of 20 watts, with a current range of 7 to 30 amps. The pulse frequency ranges from .1 to 1.0 kHz. To maintain an operating temperature between 27°C and 32°C, the laser is cooled by an external water chilling unit. The laser output is controlled by a remote control unit. Because the laser is not able to interface with a computer, the laser pulse was not synchronized with the camera. However, the pulse width of the laser was sufficiently long so that this did not pose a problem. After the laser beam exits the laser housing, it is redirected to the measurement area in the test section by a series of lenses and mirrors that are easily adjusted to accommodate many configurations. The beam is first concentrated and then spread into a triangular plane in order to create a plane of illumination perpendicular to the surface of the object in the test section.



Figure 3.3 Quantronix Falcon 30 series Nd:YLF laser

For data acquired more recently, a Quantronix Darwin 527-30-M laser was used (Figure 3.4). This laser generates a beam width of 527 nm. Like the Falcon laser, the laser pulse was not synchronized with the exposure of the camera. However, because the pulse width of the beam is significantly long compared to the camera exposure time, this was not an issue. The pulse rate on this laser ranges from .1 to 10 kHz. This laser was much more reliable than the Falcon laser as the running temperature stayed relatively constant. It also was able to provide greater illumination of the particles, which improves the PIV image processing.



Figure 3.4 Quantronix Darwin-527-M laser head

The camera used to obtain the raw PIV images was a Basler A504k 8-bit high-speed digital camera with a Nikon AF Micro Nikkor 105mm lens (Figure 3.5). The camera is capable of acquiring images at a maximum frame rate of 500 Hz with a resolution of 1280x1024 pixels. The camera was mounted underneath the test suction of the water tunnel in order to capture the illuminated plane (Figure 3.6). The lens is manually focused in order to obtain the best images of the particles. The camera can also be raised and lowered to take data over a range of window sizes. The size of the image capture area is evaluated by taking a calibration image using a ruler placed in the laser sheet. The camera is connected to a PC by a National Instruments PCIe-1429 frame grabber, which worked in conjunction with a LabView program to capture and store the

images in TIFF format. For each unique configuration (free stream speed, angle of attack, image location) 4800 images were taken during experimentation. To avoid memory allocation problems and software crashes, this was done in 4 sets of 1200 images. The images are then paired using a LabView program in order to be correctly input into the PIV processing software. Insight 3G required that each image be paired with its successive image so that a velocity vector can be calculated using the timestep between the images. For processing purposes, image 1 and 2 are converted to 1A and 1B, images 2 and 3 are converted to 2A and 2B, and so forth. These paired images are then imported into the PIV processing software.



Figure 3.6 Basler A504k 8-bit high-speed camera with Nikon AF Micro Nikkor 105mm lens.

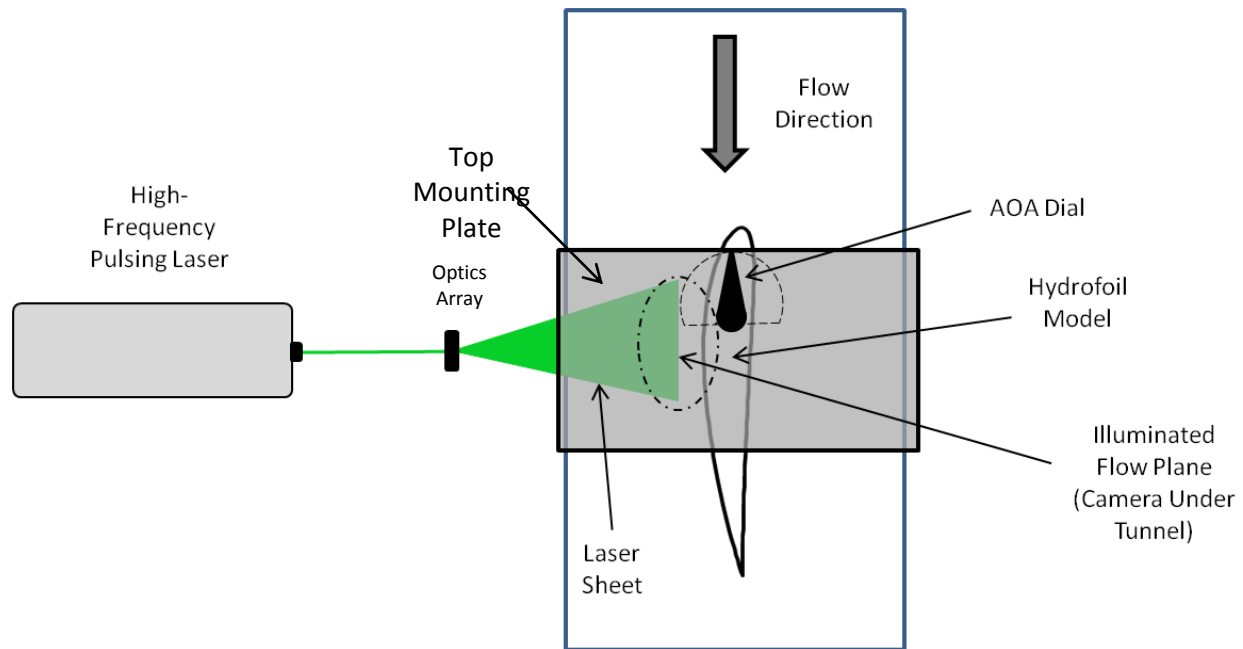


Figure 3.5 Top-down diagram of experimental setup in water tunnel test section.

PIV processing and preliminary analysis was performed was performed using Insight 3G and Insight 4g, PIV software programs developed by TSI, Incorporated. Using the TIFF format image pairs, the software computes the resulting vector fields for each run of 1200 images given a user input time and length scale. A mask can be applied to the processing window. This prevents the software program from creating gradients at the edge of the image region or from calculating vectors in regions where there is no particle motion, helping to decrease processing time. The software tracks the particles in the images by dividing the image frame into a grid of interrogation windows. The size of these interrogation windows can be altered by the user according to the application. The smaller the interrogation window size, the better the resolution of the vector field. However, an optimal interrogation window size that balances resolution and vector quality can be determined. The software has several pre- and post-processing options such as image contrast enhancement, local and global vector validation, and vector interpolation. In

this experiment, a pre-processor to enhance the background to particle contrast was used. A post-processor for local vector validation and vector interpolation was used to remove erroneous vectors that were generated and to also fill in areas with missing vectors. The computed vector fields are then imported into MATLAB. Several parameters of interest can then be calculated from the vector files.

### 3.3 EXPERIMENTAL MODELS

Two models were used for the study of the separation control effects of mako shark skin. The first model was a left pectoral fin from a Shortfin Mako shark. The fin measured approximately 71 cm from root to tip with an average chord of 15 cm. The Shortfin Mako from which the pectoral fin was removed was obtained from commercial fisherman off the coast of Montauk, New York (Motta et al., 2012). The shape of the cross-section of the fin at the location tested was traced and found to most closely agree with that of a NACA 4510 airfoil. The fin was then cleaned with tap water and frozen until being mounted in the apparatus. When not in use, the fin is kept frozen. To hold this fin securely in place, an aluminum mounting bracket was affixed to the root of the fin by means of two stainless steel rods that are embedded in the cartilaginous structure of the fin (Figure 3.7). To allow for the control of the angle of attack of the shark fin, as well as keep the fin mounted vertically in the water tunnel, the mounting bracket was made to attach to a previously fabricated aluminum plate that rests over the top of the test section of the water tunnel. This plate is clamped to the top surface of the tunnel to keep the model submerged as well as from moving during testing. Tick marks were etched into the top aluminum plate so that the airfoil could be set at any angle of attack from -90 degrees to +90 degrees in increments of one degree. The mounting system positions the chord line of the fin at the midpoint of the tunnel width in order to maximize the distance between the surface of the fin

and the tunnel walls (Figure 3.8). After measurements were taken over the natural pectoral fin, the fin was then sealed with spray adhesive and painted with a latex based paint in order to cover the scales and prevent their erection.



Figure 3.7 Left pectoral fin attached to mounting bracket.

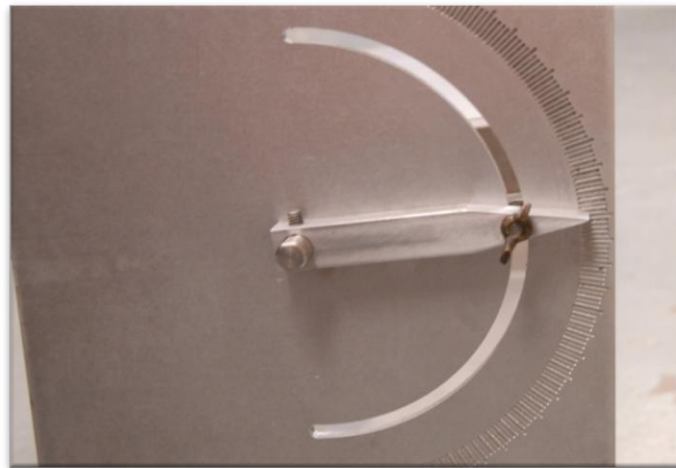


Figure 3.8 Angle of attack dial for pectoral fin mounting bracket.

The other model used was a PVC cylinder to which shark skin was attached. The cylinder has a diameter of 8 cm and a length of 36 inches. The length of the cylinder was chosen so that the cylinder would span the entire depth of the test section to reduce end-effects of a finite length cylinder placed in the water tunnel. The cylinder was mounted in the test section using an aluminum mounting bracket affixed to an aluminum plate. Once again, the aluminum plate was

clamped to the top of the water tunnel to keep the cylinder from moving during experimentation. The cylinder with the mounting configuration can be seen in Figure 3.9.

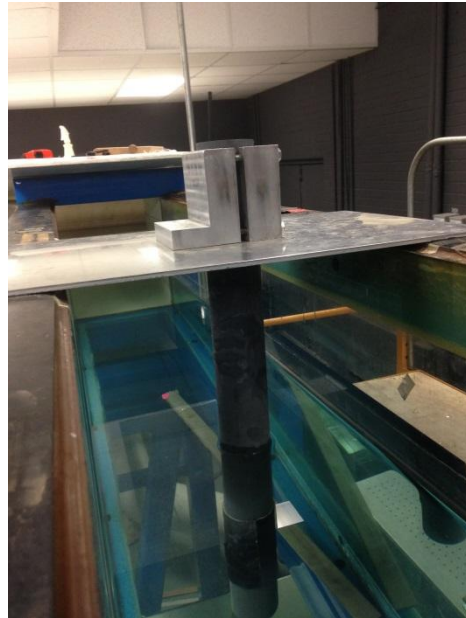


Figure 3.9 Cylinder and mounting bracket in water tunnel test section.

Two cylinders were used in this experiment. The first model used was a smooth cylinder. This was done in order to obtain baseline data for a smooth cylinder. The data obtained can be compared to historical data, which is widely available and studied. The other cylindrical model involves the application of Shortfin Mako shark flank skin. Over a 7 inch length of the span of the cylinder, the diameter was decreased by 5mm. This was done to account for the thickness of the shark skin to be applied. This length of span was chosen because the maximum width of usable skin from the flank sample was approximately 7 inches. Two rectangular sections of skin were applied around the circumference of the cylinder with the scales directed in the downstream direction. Two pieces were used because the scales have a preferential flow direction. Using one continuous piece would cause scales on one side of the cylinder to be oriented in the wrong direction. Skin was used from the flank section for two reasons: the flank section has the least amount of body curvature allowing for flat samples and the scales at this location have the

highest range of scale flexibility, which may allow for the highest degree of separation control. The two samples were joined at exactly the leading edge and trailing edge of the cylinder. Much care was taken when applying the skin so that these seams would be smooth as to not disturb the flow over the cylinder. Figure 3.10 shows both cylindrical models: plain cylinder and cylinder with applied Shortfin Mako shark skin.



Figure 3.10 Smooth PVC cylinder (left) and PVC cylinder with attached shark skin (right)

It is important to note that the skin was not able to be cut extremely precisely. This is due to the orientation of collagen fibers within the skin. The skin samples applied to the cylinder were also chosen because of the uniformity of the thickness. No large protrusions were present in the skin samples. To ensure a uniform thickness around the circumference of the cylinder, the underside of the skin samples was shaved in some locations where the thickness varied.

Because the skin is a biological material, care must be taken in preserving the integrity of the skin and the scales. In order to preserve the skin, both the pectoral fin and the cylinder with

the applied skin were stored in a freezer when not in use. Before use, the skin was allowed to thaw to room temperature while sitting in the water tunnel before experiments were run. The skin samples can be thawed and refrozen between 5-8 times before the scales become damaged and loose (Motta, personal communication). In order to avoid such damage, the experiments run with the models with the skin samples were done over a few days. This allowed much data to be taken while only thawing and refreezing twice. The scales can also be damaged if they come into contact with other objects. Therefore, during handling and installation, it was important to not touch the skin by hand or make contact with other objects.

### 3.4 EXPERIMENTAL PROCEDURE

In order to obtain a wide range of data over several experimental conditions, PIV measurements were taken at various angles of attack, speeds, and locations on the models. The measurement locations were laid out so that the entire chord length of the models could be analyzed. Between the data locations, some overlap was present in order to accurately piece together the data from each location. For both the pectoral fin and the cylinder models, two chordwise measurement locations were used, the first of which included the leading edge and the midpoint and the second included the midpoint and the trailing edge. For the pectoral fin, a field of view of approximately 70x60 mm was used while over the cylinders, a field of view of approximately 65x52 mm was used. Schematics of the measurement locations for the fin and the cylinder are shown in Figure 3.11. A large field of view was also used. This field of view includes the top right quadrant of the cylinder and approximately one diameter length into the wake of the cylinder.

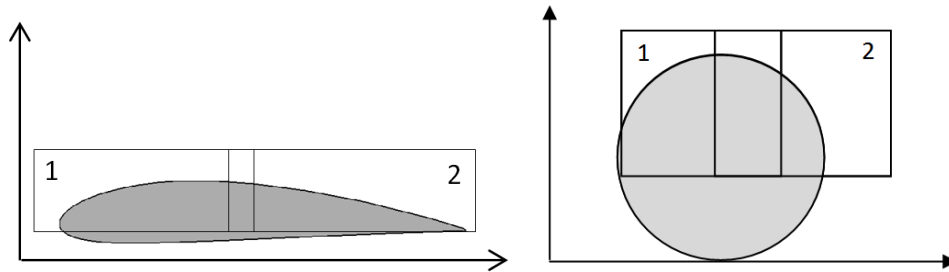


Figure 3.11 Measurement locations for pectoral fin (left) and cylinder (right).

In the case of the pectoral fin, the angle of attack was varied, along with the free stream speed of the water tunnel. The angles of attack used were 0, 4, 6, 8, and 12 degrees. For each angle of attack, the free stream speed of the tunnel was also varied. The speeds used were 0.327 m/s and 0.5 m/s. These speeds correspond to pump motor frequencies of 40 Hz and 60 Hz, which, as previously mentioned, can be correlated using the calibration chart (Figure 3.1) which was created using a particular water height in the tunnel. In order to keep this same calibration, the water level must be adjusted to this specific level before the tests are run. For the tunnel speeds of 0.327 m/s, the camera and laser were set to 400 Hz and for a tunnel speed of 0.5 m/s, the camera and laser were set to 500 Hz. These free stream tunnel speeds correspond to Reynolds numbers based on the chord of 55,000 and 86,000, respectively. The camera was aligned along the surface of the pectoral fin. In order to minimize the movement of the laser optics and camera setup, each parameter was tested consecutively. For example, at each angle of attack, the data was taken for both free stream speeds. After measurements were obtained for all speeds, the angle of attack was changed and the camera was then moved to reflect that change of angle of attack.

In the case of the cylinder models, only the speed and the measurement locations were altered. The free stream speeds tested were 0.247 m/s, 0.327 m/s, and 0.5m/s. Once again, these

speeds were determined using the calibration curve for the water tunnel speed. These free stream speeds correspond to Reynolds numbers based on the diameter of 22,400, 29,400, and 45,000. For the cylinders, the camera was aligned in the x- and y-direction of the water tunnel test section, opposed to the surface alignment for the pectoral fin. After each speed was taken at a single location, the camera was moved to the next location and the process was repeated.

After four runs of 1200 images per run for each unique measurement condition, the images were converted using a mass conversion program written in LabView. Each individual run was then loaded into the Insight 3G software to be setup for processing. A processing mask was applied to mask out regions of the image that were below the surface of either the pectoral fin or the cylinders. Before processing the cylinder data, the images needed to be enhanced to allow for better particle detection. This was determined after preliminary processing did not yield reliable results. In order to enhance the images, a background subtraction was used. The background subtraction uses several images to get an average background light intensity. This average intensity is then subtracted from all the images, effectively increasing the contrast between the particles and the background of the images. For all cases run, the processor within Insight 3G was set to use a recursive Nyquist grid. The grid size was changed between the tests at different speeds to allow for the maximum number of “good” vectors to be determined by the processing software. The recursive grid allows for an initial interrogation window size to be set. After the particle movement has been analyzed in this initial size window, the particle motion is analyzed in a smaller interrogation window. This helped to improve the x- and y-direction resolution. The maximum particle displacement was set to 50% of the interrogation window width for all cases. For the cases with a free stream speed of 0.247 and 0.327 m/s, the  $\Delta t$  parameter was set to 2500  $\mu\text{s}$ . This number is based on the pulse and capture rate of the laser and

camera and goes into the calculation of the velocities found in the measurement field. For the higher free stream speed of .5 m/s, the parameter delta t was set to 2000  $\mu$ s.

In addition to applying a mask and setting the time scale for processing, the length scale for each location must be entered into the processing software. This length scale is measured by means of a calibration image. A calibration image was taken each time the camera was moved. This accounts for any enlargement or constriction of the measurement window. A ruler is placed in the measurement window and a still image is taken. Using image editing software, such as MS Paint, the number of pixels in a given length can be determined. The processing software requires input in units of  $\mu$ m/pixel, which is simply the inverse of the previously found number. The length scales used for calibration as well as the image sizes are displayed in Table 3.1.

Application	Length Scale ( $\mu$ m/pix)	Field of View (mm)
Cylinder	51.24	65.59 x 52.47
Pectoral Fin	55.7	71.3 x 57.04

Table 3.1 Length scale calibration and field of view of processed images.

After each experimental run is processed, the images are then loaded and averaged with the other runs from the same configuration using MATLAB programs. These programs analyze the velocity field data and allow for plots such as average backflow magnitude and backflow coefficient to be created.

## 4. RESULTS AND DISCUSSION

The following sections outline the results obtained for both the Shortfin Mako shark pectoral fin as well as the cylinder model. Parameters that are averaged have been done so over 4800 image pairs, or 12 seconds of data. This number was determined to be the optimal number for processing because it provided a true average for the flow at hand. To verify that the results used were the true average, two additional runs were taken for several cases. These runs were averaged so that the total number of images was 6000. It was found that beyond 4800 images, adding more images did not change the contours generated for each case. To avoid excessive processing time, the total number of samples used for processing in each case was kept at 4800.

### 4.1 SHORTFIN MAKO PECTORAL FIN

The following section outlines the results obtained over the pectoral fin from the Shortfin Mako shark. All results obtained were averaged over 4800 images. When taking data, the camera had to be moved to align with the surface for each angle of attack. Also, when the free stream speed of the tunnel was increased, the fin flexed due to lift being produced. Because of this reason, the surface of the fin does not always correspond between data obtained at different angles of attack and different free stream speeds ( $Re$ ).

#### 4.1.1 BACKFLOW COEFFICIENT

Backflow coefficient contour graphs were generated with MATLAB using the vector files created by the Insight 3G PIV software. Backflow is defined as flow having a negative u-component. The backflow coefficient is defined as the percentage of the total run time that flow is moving in the negative u-direction. These graphs were generated for all cases where backflow occurred at least 10% of the total run time. When calculating the backflow coefficient, the validity of each vector was checked before adding it to the calculation. If a vector was found to be invalid, it was disregarded for this calculation. The contours of 10% and 50% backflow are commonly used to compare the cases.

As previously stated, both the natural fin and the painted fin were run at various angles of attack at two Reynolds numbers, 55,000, and 86,000. At the lower angles of attack, not much difference was observed between the two surface configurations. Over both surfaces, little to no backflow or separation was observed. This was the case for both Reynolds numbers at the lower angles of attack. For example, backflow coefficient contours for both surface configurations at an angle of attack (AOA) are shown below. Figure 4.1 shows the backflow coefficient contours of the two surface configurations at a Reynolds number of 55,000 while Figure 4.2 shows the same at a Reynolds number of 86,000. From both of the figures below, it can be seen that there is almost no difference in the separated region when comparing the natural fin to the painted fin. A contour of 50% backflow was not observed over either of the two surface configurations. While the contours do not exactly match, such small differences are negligible.

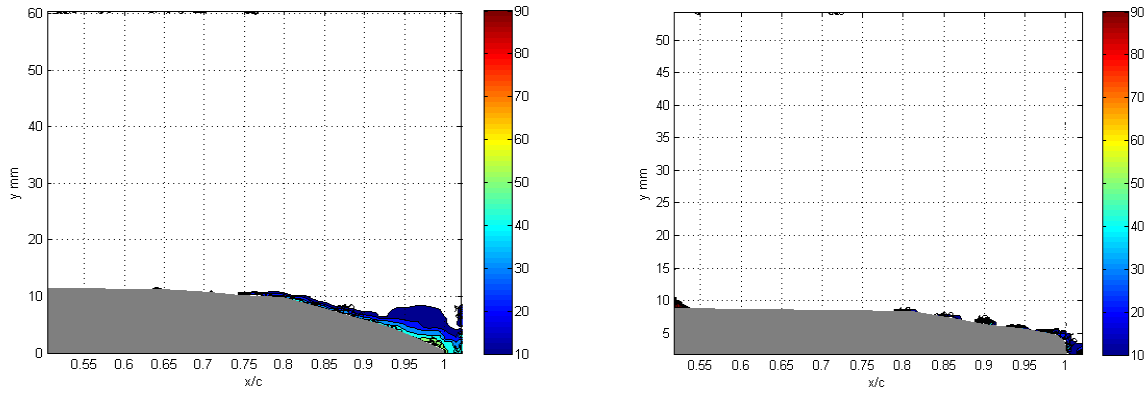


Figure 4.1 Backflow coefficient contours,  $Re=55,000$ ,  $\alpha=4^\circ$ . Painted (left) vs. natural fin (right).

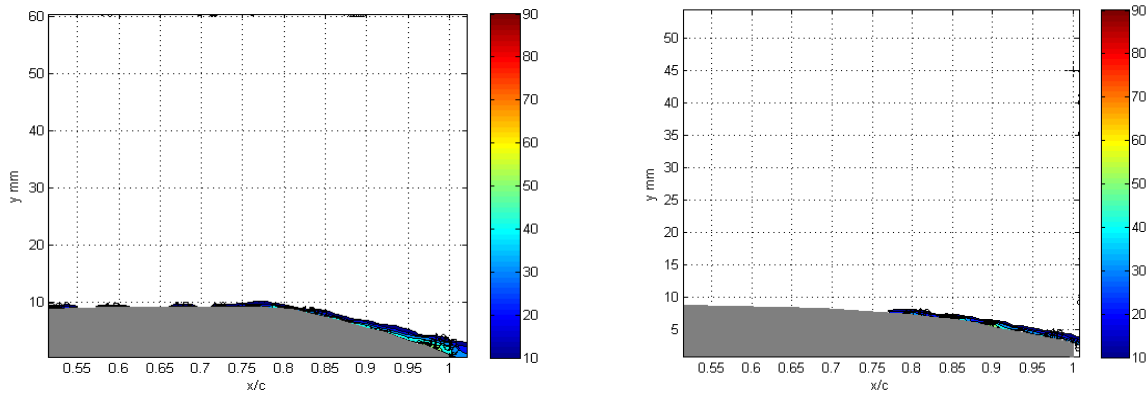


Figure 4.2 Backflow coefficient contours,  $Re=86,000$ ,  $\alpha=4^\circ$ . Painted (left) vs. natural fin (right).

At higher angles of attack, differences were observed between the two surface configurations as well as between the surfaces run at different Reynolds numbers. For instance, at  $\alpha=8^\circ$ , a difference is noted between the two surfaces at a Reynolds number of 55,000. This case is presented below in Figure 4.3. For this case, the length of the backflow region grew on the painted surface (backflow present forward of  $.5 x/c$ ). However, over the natural fin, only 10% backflow is encountered at the trailing edge, suggesting that the scales help to mitigate the reversing flow and delay flow separation.

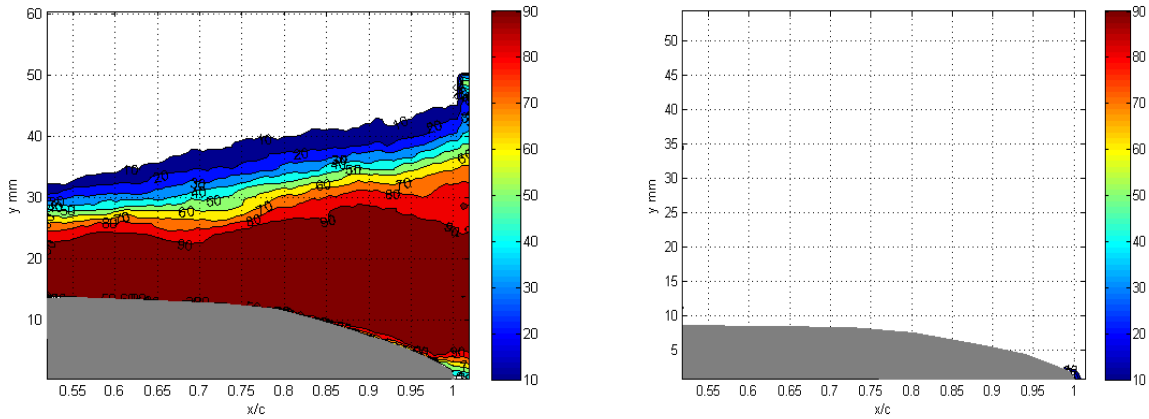


Figure 4.3 Backflow coefficient contours,  $Re=55,000$ ,  $\alpha=8^\circ$ . Painted (left) vs. natural fin (right).

A general increase in the thickness of the separated region was observed when the angle of attack of the pectoral fin was increased. Backflow was also observed to occur a greater percentage of time as the angle of attack was increased. This is seen when comparing Figure 4.2 and Figure 4.5, as well as the contours for other angles of attack. As the angle of attack is increased, the contours of larger reversing flow percentage are seen to cover a larger portion of the separated region.

One notable aspect that was observed was over the natural fin at  $AOA=12^\circ$ . At the lower Reynolds number, 90% backflow is observed adjacent to the surface that originated in region 1 and extends to  $x/c=0.97$   $x/c$  on both the natural and painted surfaces. The contour of 50% backflow also originates in region 1 for both surfaces and is approximately 20 mm above the surface at  $x/c=0.55$ . However, when both surface configurations are subjected to a higher free stream velocity, comparing the two surfaces reveals that backflow is occurring more often for the case of the painted fin. Figure 4.4 shows the backflow coefficient contours at  $\alpha=12^\circ$  and  $Re=55,000$  for both the painted and natural fin. This figure shows that while the separated region

over the natural fin is slightly smaller in size, the two regions are somewhat similar, with contours of 90% backflow terminating approximately at  $x/c=0.97$ . One possible explanation for this phenomenon is the presence of 3-dimensional flow at the higher speeds. Figure 4.5 depicts the backflow coefficient contours for  $\alpha=12^\circ$  and  $Re=86,000$ . Over the natural fin, relatively little backflow is encountered, while a large separated region is present over the painted fin. Backflow is occurring a maximum of 20% of the time over the natural fin while areas of over 90% backflow are observed to occur over the painted fin. This finding suggests that the scales require a certain magnitude of backflow, or shear, to become bristled and mitigate the reversed flow. This phenomenon is further investigated using the average backflow magnitude.

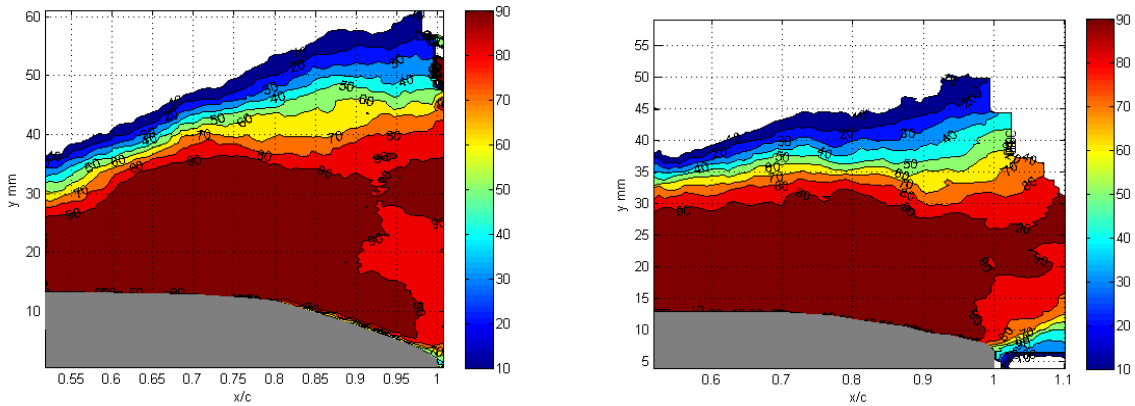


Figure 4.4 Backflow coefficient contours,  $Re=55,000$ ,  $\alpha=12^\circ$ . Painted (left) vs. natural fin (right).

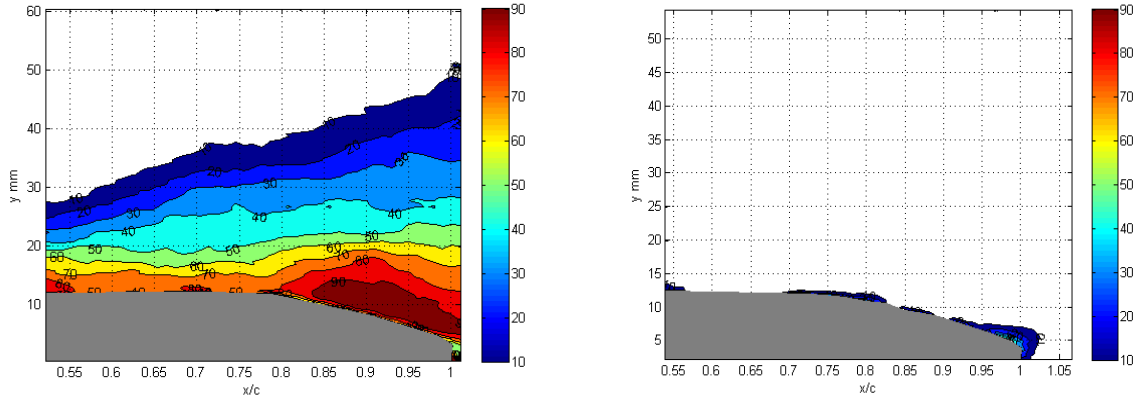


Figure 4.5 Backflow coefficient contours,  $Re=86,000$ ,  $\alpha=12^\circ$ . Painted (left) vs. natural fin (right).

#### 4.1.2 AVERAGE BACKFLOW MAGNITUDE AND PEAK BACKFLOW MAGNITUDE

Contours of the average magnitude and peak backflow magnitude of the backflow were generated in MATLAB for all cases where backflow was observed. The backflow was averaged for each case over the total number of instantaneous velocity vectors at each grid location in the processing window. The average magnitude of the reversing flow is analyzed for all cases where differences were observed between the backflow coefficient plots.

Figure 4.6 shows the average backflow contours for  $Re=55,000$  at  $\alpha=8^\circ$ . Over the painted fin, contours of backflow magnitudes greater than .1 m/s were observed to originate at  $x/c=.5$  while the peak average backflow was observed to be at  $x/c=.66$ . However, no backflow is seen over the painted fin. Because little to no backflow was observed over the natural fin, this indicates that the backflow that would be present, as in the case of the painted fin, is sufficient to bristle the scales. The scale bristling prevents the boundary layer from separating in this case. Figure 4.7 shows the peak backflow magnitude for this case. Peak backflow magnitudes of approximately .25 m/s are encountered along the surface for the painted fin.

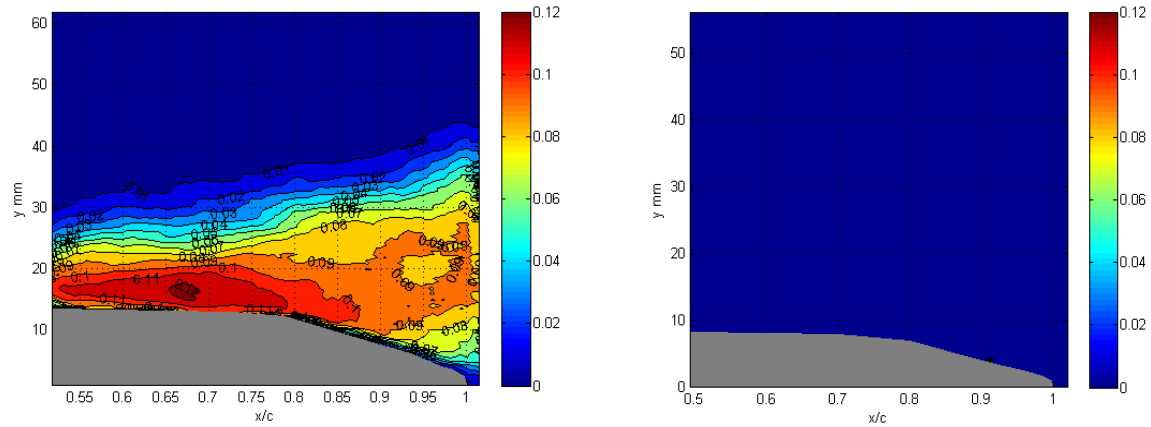


Figure 4.6 Average backflow magnitude contours (m/s),  $Re=55,000$ ,  $\alpha=8^\circ$ . Painted (left) vs. natural fin (right).

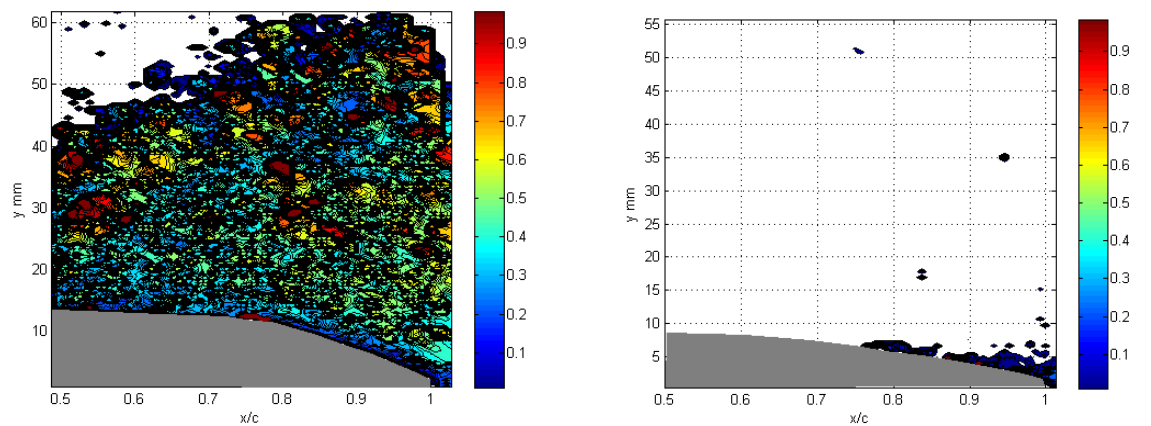


Figure 4.7 Peak backflow magnitude,  $Re=55,000$ ,  $\alpha=8^\circ$ . Painted (left) vs. natural fin (right).

The average backflow magnitude contours are compared below for  $\alpha=12^\circ$ . For  $Re=55,000$  (Figure 4.8), the backflow coefficient plot revealed that when averaged over time, backflow occurs over both surfaces. The area and amount of time over which backflow is present are very similar at this lower Reynolds number. When comparing the average backflow magnitude for  $Re=55,000$ , it can be seen that the same is occurring. Over both surfaces, a maximum average backflow of 0.1 m/s is encountered. It is also interesting to note that the location of the maximum averages are equivalent for the two cases. It is important to note in these figures that the scale has

been adjusted for each case according to the locally encountered values for the smooth surface. In every case, the maximum occurring backflow magnitude for the natural fin was less than or equal to that over the painted fin. However, for the case presented below, the area corresponding to 0.1 m/s average backflow is larger over the natural fin than over the painted fin. Peak backflow magnitudes for this case show that the peak backflow magnitude encountered at the surface is approximately .2 m/s. This is 20% less than the previous case, which may explain the negligible effect of the shark skin on mitigating flow separation.

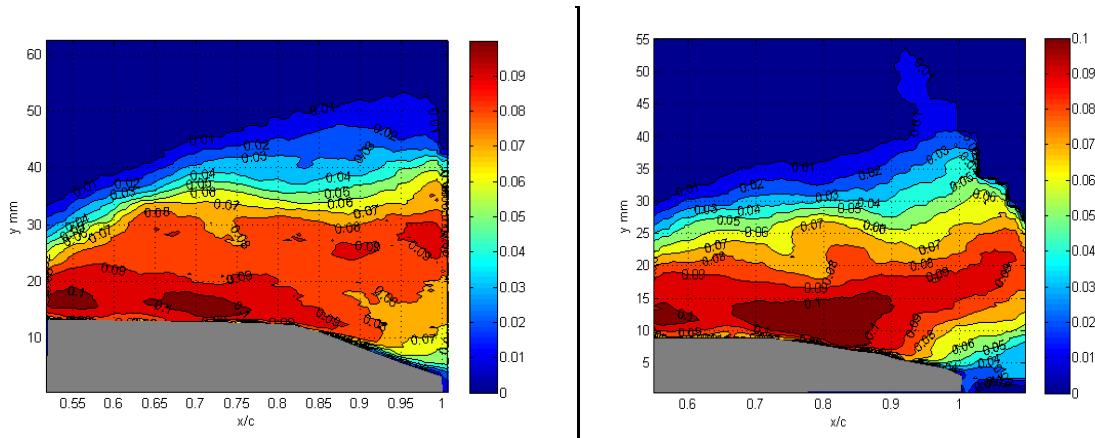


Figure 4.8 Average backflow magnitude contours (m/s),  $Re=55,000$ ,  $\alpha=12^\circ$ . Painted (left) vs. natural fin (right).

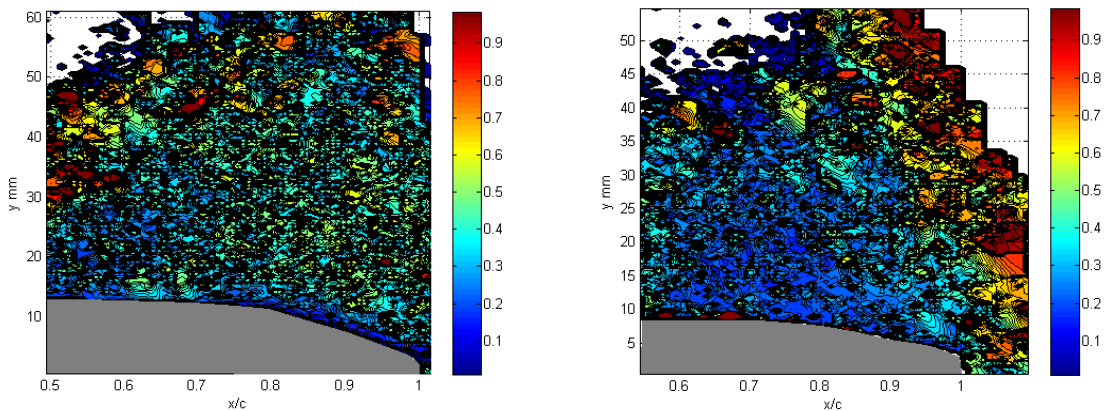


Figure 4.9 Peak backflow magnitude,  $Re=55,000$ ,  $\alpha=12^\circ$ . Painted (left) vs. natural fin (right).

At  $Re=86,000$  (Figure 4.10), the differences between the flow characteristics over the two surfaces become significantly greater. The painted surface encounters a maximum average backflow magnitude of approximately  $.12$  m/s. This magnitude of reversed flow originates at a point near  $x/c=.82$ . Average backflow with magnitude of  $.1$  m/s continues over the surface until very near the trailing edge. For this higher Reynolds number, a small area of backflow with magnitude of  $0.02$  is seen at  $x/c=0.8$ . This is the highest average backflow magnitude encountered over the natural fin. Little to no backflow present over the natural fin suggests that some aspect of the surface has effectively impeded the reversing flow. This impedance keeps the boundary layer attached to the surface of the fin. It can be seen that the magnitude of reversing flow encountered over the painted fin was enough to bristle the scales which extend into the boundary layer and limit the flow reversal. The average backflow magnitude contours for  $\alpha=12^\circ$  and  $Re=86,000$  are shown in Figure 4.10. Peak backflow magnitude contours (Figure 4.11) show that the peak backflow magnitude found near the surface over the smooth surface was found to be on average  $.35$  m/s. Comparing this to the peak values found on the surface for  $Re=55,000$  and  $\alpha=12^\circ$ , the higher peak magnitudes may explain why flow separation is minimized over the shark skin at the higher Reynolds number.

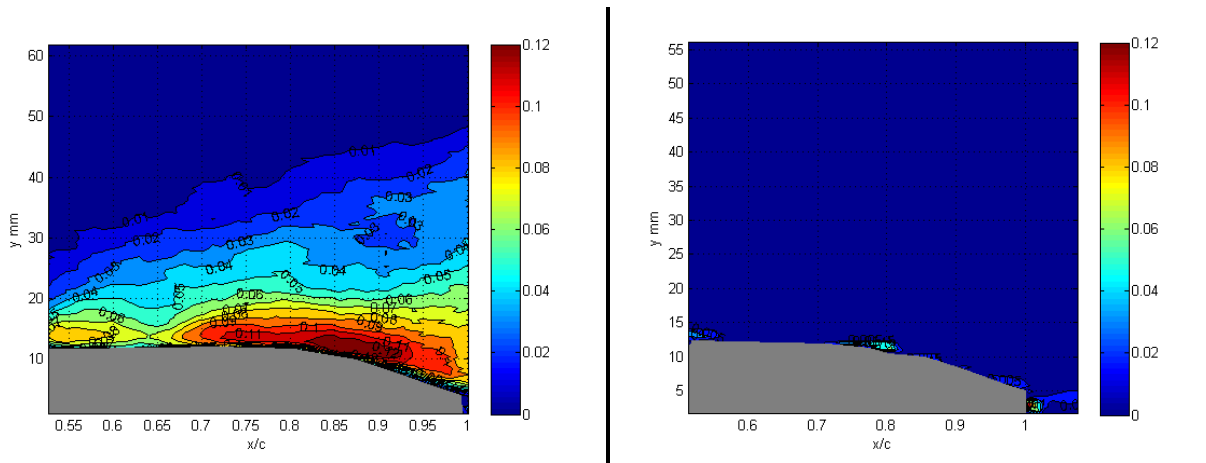


Figure 4.10 Average backflow magnitude contours (m/s),  $Re=86,000$ ,  $\alpha=12^\circ$ . Painted (left) vs. natural fin (right).

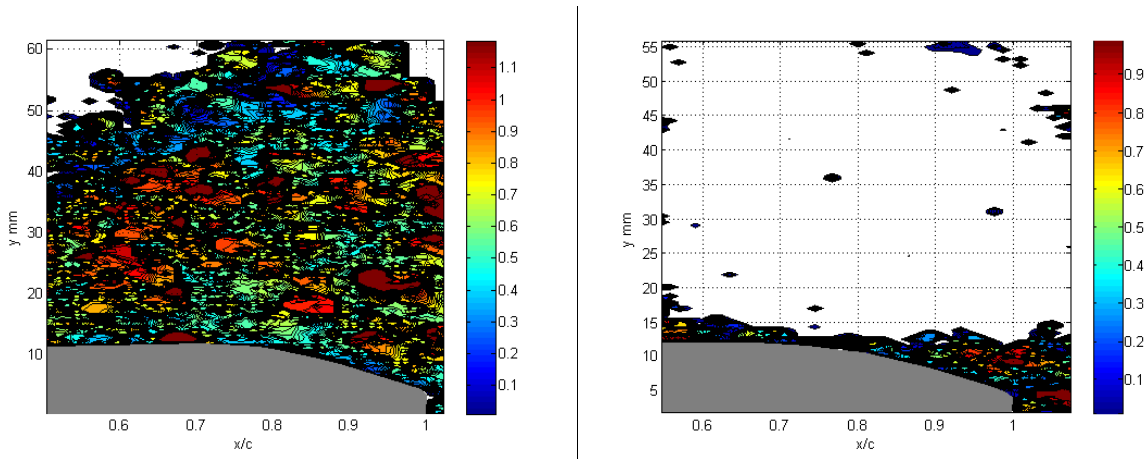


Figure 4.11 Peak backflow magnitude,  $Re=86,000$ ,  $\alpha=12^\circ$ . Painted (left) vs. natural fin (right).

## 4.2 CLYINDER

The following section outlines the results obtained over the cylinder with both a smooth surface and with applied shark skin. All results obtained are averaged over 4800 images. Data was obtained for Reynolds numbers based on diameter of 22,400, 29,400, and 45,000. These Reynolds numbers correspond to water tunnel free stream speeds of 0.247 m/s, 0.327 m/s, and .5

m/s, respectively. In addition to the plots that are presented below, a drag approximation was also performed to further analyze the effectiveness of shark skin in controlling flow separation. The results compared in this section focus primarily on those obtained in the second image location which can be seen in Figure 3.11 in the Experimental Configuration section. The parameters presented are given in both Cartesian and polar coordinates for clarity.

#### 4.2.1 BACKFLOW COEFFICIENT

Backflow coefficient plots were compared for all Reynolds numbers over the 2 cylinder configurations. For the backflow coefficient over the cylinder, this parameter is presented in two ways. For one set of plots, the flow is considered to be reversed if it is flowing in the negative x-direction. For the other set of plots, backflow is defined as where the flow is moving tangential to the cylinder against the direction of the free stream flow. For example, over the top half of the cylinder, backflow is defined as flow moving in the direction of the counterclockwise theta direction. The backflow coefficient allows for the average point of separation over time to be seen. Plotting the backflow coefficient in polar coordinates shows the backflow that is occurring tangential to the surface at all points in the flow. The flow that is tangential to the surface is directly related to the shear that the surface encounters. While plots using both methods have been generated for all cases, this section primarily focuses on the polar configuration.

The results from the cylinder at a Reynolds number of 22,400 are shown below in Figure 4.9 and Figure 4.10. From the plot on the left of Figure 4.9 it can be seen that the size of the first contour line originated from a point approximately 5% of the diameter of the cylinder. It can also be seen that the thickness of the region of backflow far from the trailing edge of the cylinder is

decreased when the sharkskin is applied. At a distance of  $1.2 x/d$ , the area of reversed flow has a height of  $1.05 x/d$ , meaning it extends approximately  $0.4 \text{ cm}$  past the top of the cylinder. This is compared to the cylinder with the applied shark skin (shown at the right), where the height of the reversed region at the same location only extends to  $0.97 x/d$ , remaining in the shadow of the cylinder. While the origin of the backflow contours is approximately the same for both cylinder configurations, it is evident that higher degrees of backflow, i.e. 50%, occur further along the surface of the sharkskin cylinder than on the smooth cylinder.

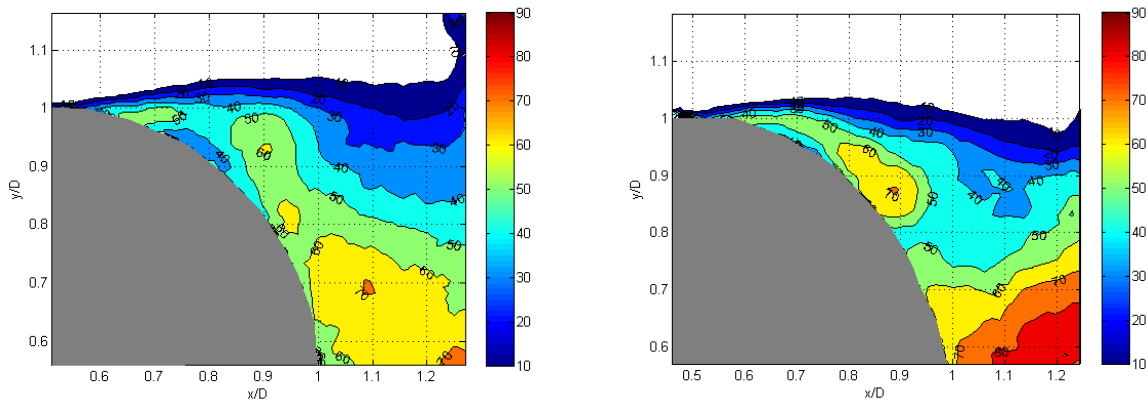


Figure 4.9 Backflow coefficient contours,  $Re=22,400$ . Smooth (left) vs. shark skin (right).

Figure 4.10 presents the polar backflow coefficient of both cylinder configurations again at the Reynolds number of  $22,400$ . As the free stream velocity, and therefore Reynolds number are increased, the general size of the separated region tends to increase. The backflow seems to occur a greater percentage of time overall. The results from Figure 4.10 can be compared to the results in Figure 4.9. It can be seen from Figure 4.10 that the size of the reversed region is slightly larger over the smooth surface than that of the shark skin surface. A backflow percentage of 70% is also seen to originate near the point of separation over the smooth surface while 70% backflow is not observed over the shark skin cylinder until  $x/D=0.75$ . One observation to note in

this figure is that the backflow coefficient directly adjacent to the surface is higher (20%) over the shark skin cylinder than the plain cylinder. Over the smooth surface, 40% backflow is encountered, while 60% is encountered on the majority of the shark skin surface. For the other two Reynolds numbers, the opposite is observed. This phenomenon is further examined with the use of the backflow magnitude. When examining the structure of the region of reversing flow, it is also interesting to note that the over the shark skin cylinder, the contours appear to be uniform, while over the smooth cylinder, the region has a complex arrangement of backflow contours.

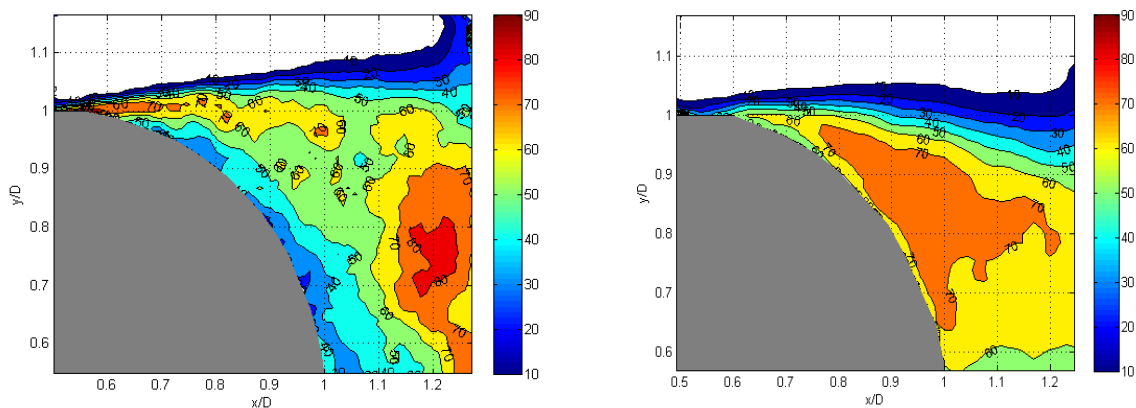


Figure 4.10 Polar backflow coefficient contours,  $Re=22,400$ . Smooth (left) vs. shark skin (right)

Similarly, the polar backflow coefficient at a Reynolds number of 29,400 is shown in Figure 4.11. Analysis of the contour of 10% backflow reveals that the point of origination on the surface with the applied shark skin is approximately the same location for both cylinder configurations. Some characteristics of the backflow region are also similar to the results at the previous Reynolds number. From the figure below, it can be seen that the height of the reversed region over the smooth surface extends beyond the data acquisition frame. However, with the applied shark skin, the height of the backflow region stays approximately level with the top of the cylinder. At this Reynolds number, however, the region of 60% and higher backflow is

significantly larger (~30%) over the smooth cylinder. Also, higher values of the backflow coefficient (90%) are observed in the case of the smooth cylinder and not over the shark skin cylinder.

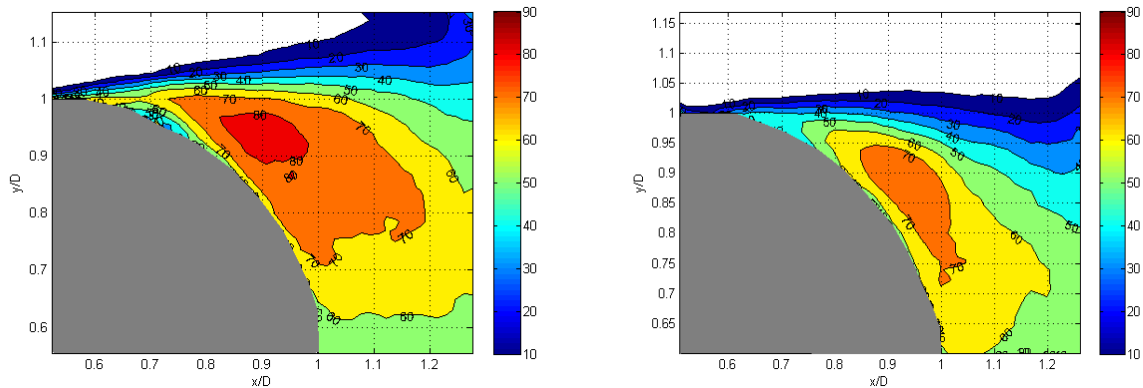


Figure 4.11 Polar backflow coefficient contours,  $Re=29,400$ . Smooth (left) vs. shark skin (right)

Flow measurements over the cylinder at a Reynolds number of 45,000 provided results that closely follow the trends outlined for the Reynolds number of 29,400. Once again, the backflow contours extend past the measurement window for the case of the smooth cylinder. A higher percentage of backflow is present on the smooth surface than on the shark skin surface. 90% backflow is encountered on the smooth surface. For instance, on the smooth cylinder, the region of 90% backflow begins at approximately  $x/D=0.7$  and extends to a point along the surface where  $x/D=0.95$ . On the shark skin surface, 90% backflow is not encountered on the surface. However, over both surfaces, the origin and end of the 70% backflow contour are equivalent.

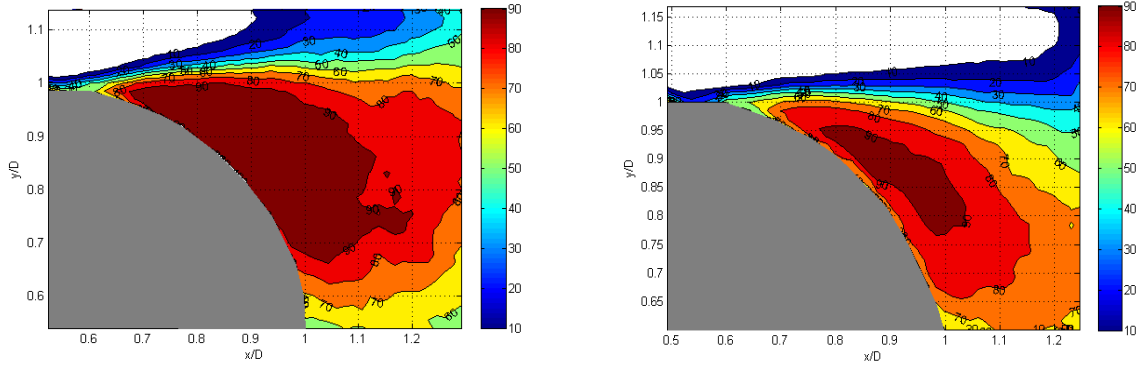


Figure 4.12 Polar backflow coefficient contours,  $Re=45,000$ . Smooth (left) vs. shark skin (right).

For all three Reynolds numbers, the backflow coefficient contours generally follow the same trends. While the point of initial separation over both surfaces is approximately the same, contours of higher backflow percentage tend to occur at a later point on the shark skin cylinder than on the smooth cylinder. Over the surface as a whole, a lesser percentage of backflow is experienced over the shark skin surface.

#### 4.2.2 AVERAGE BACKFLOW MAGNITUDE

Contours of the average magnitude of the reversed flow were generated using MATLAB. For each Reynolds number and cylinder configuration, the magnitude of the backflow was averaged over the total number of instantaneous velocity vectors. This creates a normalized magnitude that takes in to account that the flow at a certain location may not always be in the reversed direction. The plots shown below show the average backflow magnitude in the polar coordinate configuration to show the average magnitude of the reversing flow that is running perpendicular to the scales. The magnitude of the flow running tangential to the surface is directly related to the shear that the scales would undergo. If the shear and reversing momentum

are sufficient, the scales are thought to bristle, giving rise to the differences in flow characteristics. Values of average backflow magnitude are presented in meters per second (m/s)

Figure 4.13 depicts the average backflow velocity magnitude contours for  $Re=22,400$ . It can be seen from this figure that an area of higher average backflow magnitude is found over the smooth surface. The magnitude of this backflow has an average value of .08m/s in the direction tangent to the cylinder surface. Over the shark skin cylinder, the maximum backflow magnitude has an average value of 0.06 m/s. However, on both surfaces, though the magnitudes are not equivalent, the region of highest average backflow occurs at a point on the cylinder that is approximately 20 degrees above the horizontal. Over the smooth cylinder, however, a much higher backflow magnitude gradient is present at this location. The sizes of the backflow regions are approximately the same but the magnitudes of average backflow found within these regions differ. Overall, the magnitude of backflow is less. Comparing the average backflow magnitude plots to the backflow coefficient plots, it is noted that the origin of the first contour line does not match. This is due to the fact that although backflow may occur a certain percentage of the total run time, the magnitude of that backflow is small enough that it is essentially zero when averaged.

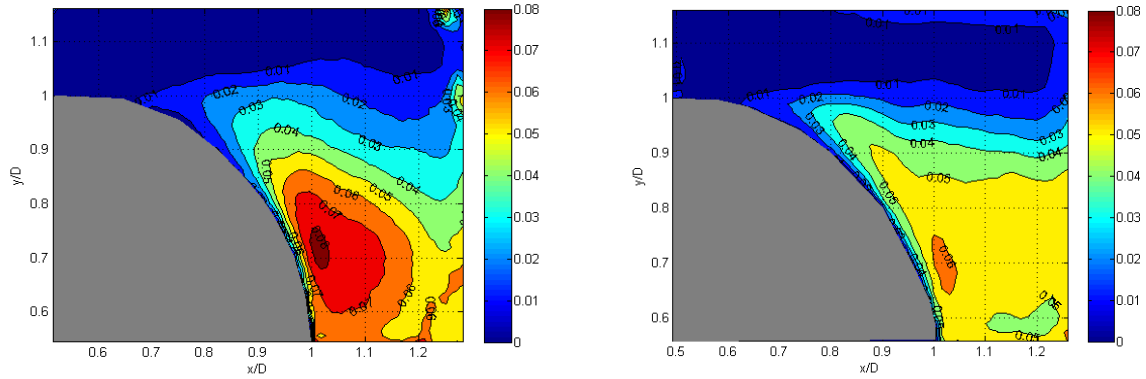


Figure 4.13 Average backflow magnitude (m/s),  $Re=22,400$ . Smooth (left) vs. shark skin (right).

Similar results were obtained for the Reynolds number of 29,400. Intuitively, as the Reynolds numbers (free stream velocity) increases, the magnitude of the backflow observed decreases. The plots of the average backflow magnitude contours are shown below in Figure 4.14, the average backflow magnitude over the smooth cylinder is again greater than that over the sharkskin cylinder. However, unlike the case for  $Re=22,400$ , the higher values of the backflow magnitude for both surface configurations seem to originate closer to the center of the wake. Over the smooth cylinder, the highest average backflow magnitude value seen encountered on the surface of 0.1 m/s is found at  $y/D=.55$ . On the shark skin cylinder the highest average backflow magnitude found on the surface of 0.07 is found near  $y/D=.6$ .

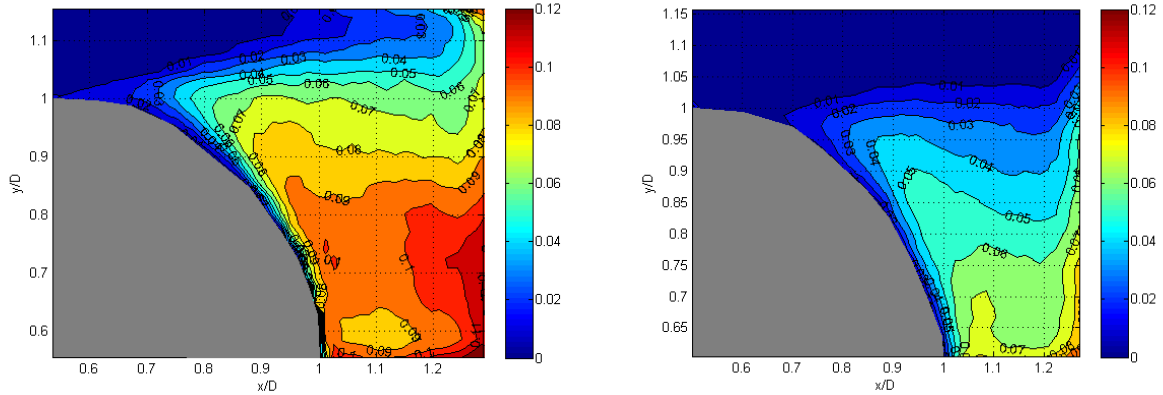


Figure 4.14 Average backflow magnitude (m/s),  $Re=29,400$ . Smooth (left) vs. shark skin (right).

For the highest Reynolds number of 45,000, the regions of high backflow magnitude seem to migrate towards the point of separation on the cylinder, which is a reversal of the trends seen between the lower Reynolds numbers. Figure 4.15 below shows the average backflow magnitude contours for  $Re=45,000$ . Compared to the results from the previous Reynolds number, the contours of the maximum values of the average backflow magnitude shifted from points near the center of the wake to points on over both surface configurations where  $x/D=0.75$ . Over the smooth cylinder, a maximum value of 0.1 m/s average backflow is seen, while small areas of 0.09 m/s average backflow are the maximum encountered over the sharkskin cylinder. Overall, the average magnitude of backflow in the wake of the shark skin cylinder is significantly less.

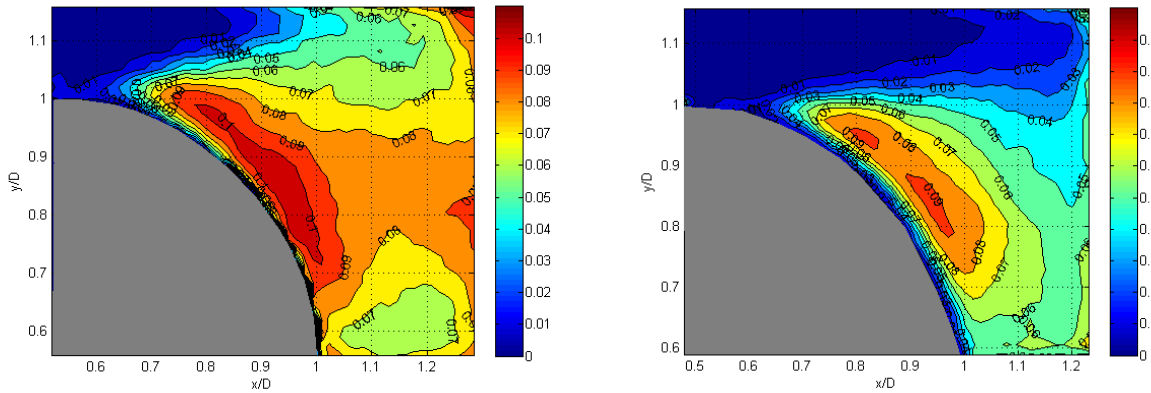


Figure 4.15 Average backflow magnitude (m/s),  $Re=45,000$ . Smooth (left) vs. shark skin (right).

### 4.2.3 VELOCITY HISTORY

A time history of the angular component of velocity at a location where  $x/D=1$  and  $y/D=0.9$  was analyzed for the different Reynolds numbers and compared over the two cylinders. It was theorized that the different surface configurations would affect the vortices shedding off the cylinder. Using instantaneous velocity plots from a point that is in the wake of the cylinder, a Fast-Fourier Transform (FFT) was run to analyze the fundamental frequencies encountered within the wake. The most notable difference between the plain cylinder and the shark skin cylinder was found at a Reynolds number of 45,000. Figure 4.16 below shows the time history of velocity for both surface configurations at  $Re=45,000$ . From this figure, it can be seen that the fluctuations of the angular component of velocity is generally less over the shark skin cylinder than over the plain cylinder. As shown previously, the average magnitude of the reversing flow is less over the shark skin surface.

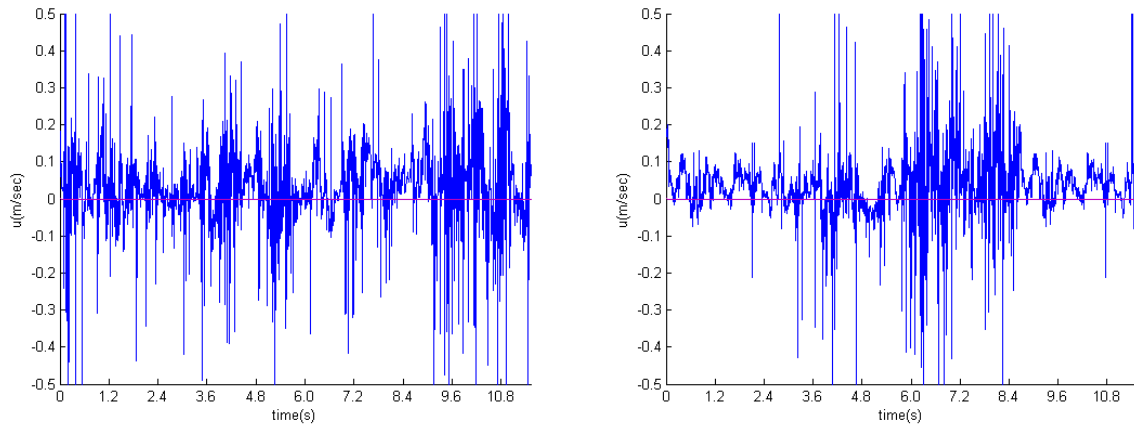


Figure 4.16 Instantaneous velocity data for plain cylinder (left) and sharkskin cylinder (right)

After performing a Fourier analysis on the instantaneous velocity data, few frequencies stood out among the rest. For the case presented above at  $Re=45,000$ , one fundamental frequency that arose for the smooth cylinder was approximately 1 Hz. For the shark skin case, the fundamental frequency was found to be approximately 1.2 Hz. The frequency predicted by theory for this cylinder is 1.1875 Hz. Therefore, with the alteration of the separation over the cylinder, the frequency at which vortices shed off the cylinder is also changed. Such a change in frequency closely agrees with the apparent thinning of the wake that is observed when the backflow coefficient is analyzed. When the flow over the sharkskin cylinder is compared to the smooth cylinder, the wake is thinner and with the thinner wake, the fundamental frequency found in the wake is slightly higher. Further investigation into this phenomenon is needed. Image tracking software would be beneficial as it can track the location of a vortex over the set of images.

#### 4.2.5 MOMENTUM ANALYSIS

Using the large area data, a momentum analysis was performed to analyze the drag over each cylinder configuration. The momentum analysis was performed by simply summing the flux over the left and right boundaries. Doing so allows the force in the x-direction (drag) to be estimated. Because the flow in the wake of the cylinder is periodic in nature, the velocities summed over the boundaries were found by averaging 4800. Using an average will allow the average drag over the cylinder to be calculated, while instantaneous drag measurements are ignored in this case. The time averaged velocity fields using the large area data for the two surface configurations are shown in Figure 4.17.

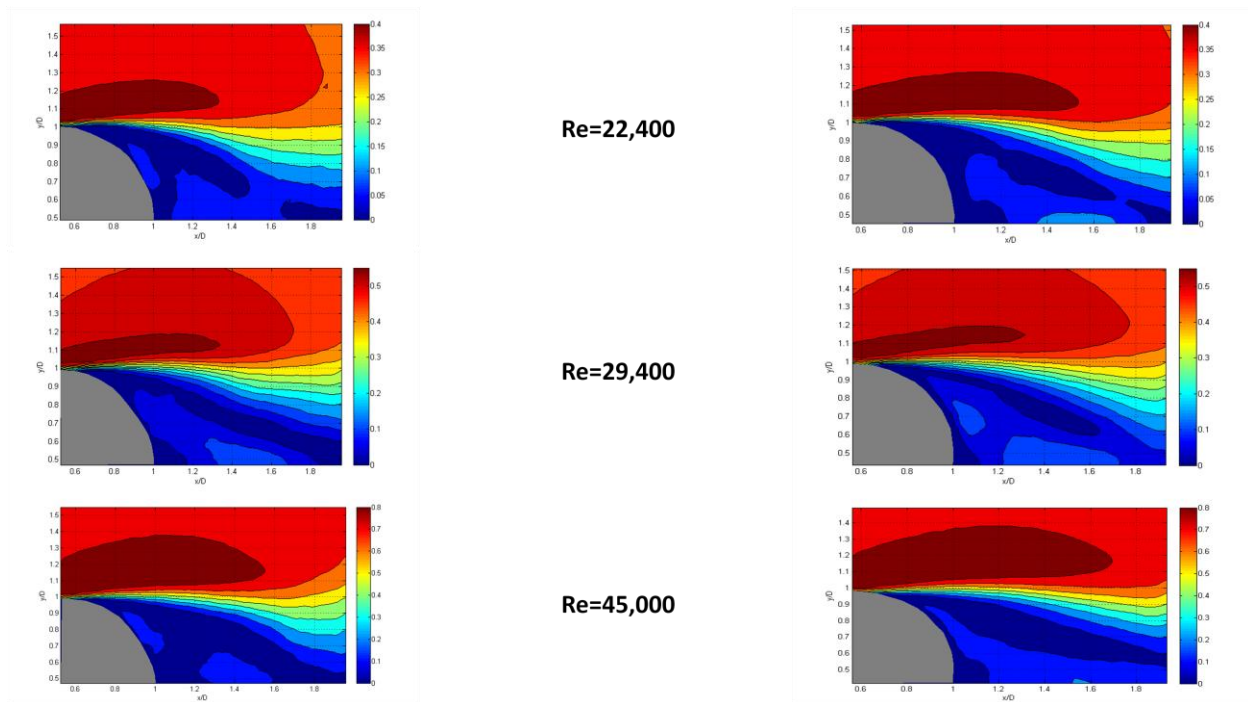


Figure 4.17 Time averaged velocity fields. Smooth cylinder (left) and sharkskin cylinder (right)

Assuming the density is constant, and knowing there is no change in area at the upstream and downstream end of the measurement window, the drag over the cylinder is proportional to

the change of the velocity crossing the left and right boundaries. This equation is shown below. Also shown below in Figure 4.18 is a sample velocity profile used to calculate the drag force. The velocity flux is summed from the midpoint of the cylinder to the top of the measurement window.

$$-F_D = \rho L \int_{-R}^R u_2(y)(U_\infty - u_2(y)) dy$$

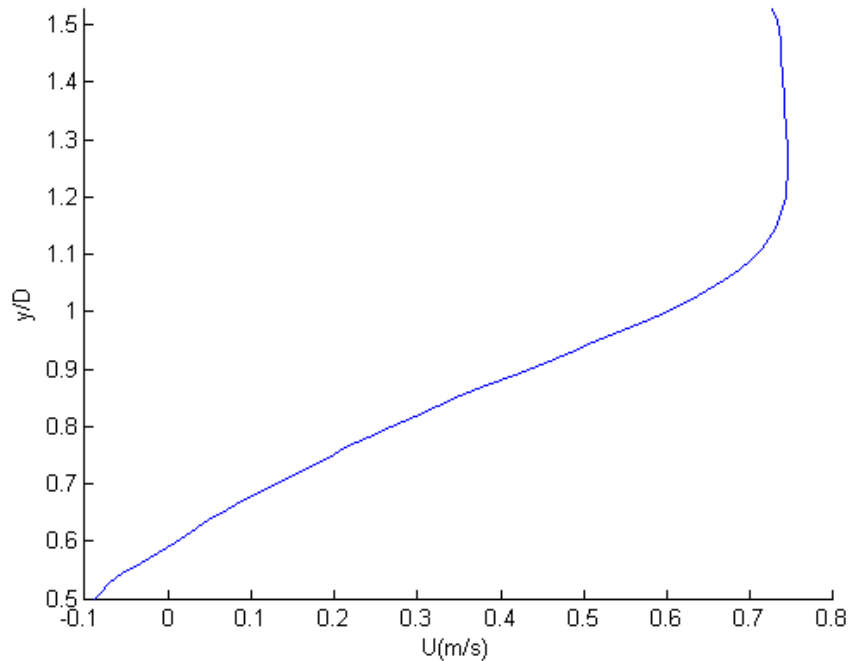


Figure 4.18 Velocity profile of downstream end of measurement window, shark skin, Re=45,000

Because only a comparison of the drag is desired between the smooth and sharkskin cylinder, an absolute measure of drag is not provided. Table 4.1 presents the simplified momentum (summed velocity) over each boundary. The percent drag reduction of applying the shark skin versus the smooth cylinder is also presented in Table 4.2. From Table 4.2, it can be seen that for all Reynolds numbers, there is an associated drag reduction when running the

cylinder with the applied shark skin vs. the smooth cylinder. Depending on the Reynolds number, the drag reduction varies from 8.59% to 31.49%. It is important to note here that this is just an estimation of the drag on the cylinder configurations. Error can arise in the calculation of the momentum flux due to poor vector calculation near the edge of the measurement window.

		Boundary	
Surface	Re	Left	Right
Smooth	22,400	14.3901	6.186304
	29,400	18.7439	-73.5492
	45,000	26.1948	-297.961
Shark skin	22,400	14.3159	7.216645
	29,400	20.1485	-107.361
	45,000	26.9259	-325.962

Table 4.1 Results of summing velocity over left and right boundaries.

Re	% Drag Reduction
22,400	14.28
29,400	31.49
45,000	8.59

Table 4.2 Percent drag reduction when shark skin is applied to cylinder.

## 5. CONCLUSIONS

### 5.1 SHARK SKIN SEPARATION CONTROL

Results obtained in this study show a noticeable difference between the flow characteristics over the surfaces with shark skin versus the smooth surfaces. For the case of the pectoral fin, analysis of both surfaces at the lower angles of attack (0, 4, and 6°) showed that the differences in the flow over the two surfaces were relatively small. This is evident in the size of the backflow region as well as the magnitudes of backflow present in the region. The location of the points of separation varies slightly between the two surface configurations, but is not significant because of the small size and magnitude of the separated region.

At the higher angles of attack (8 and 12°) many difference begin to arise when comparing the two surfaces. Differences also arise when comparing the separated flow characteristics between the different Reynolds numbers. For example, when increasing the Reynolds number at 12° angle of attack, the separated region is minimized over the surface of the natural shark fin. Only small areas of flow detachment are present, while the flow is fully separated over the painted pectoral fin. Such a drastic change is not seen at the other angles of attack when comparing the different Reynolds numbers. However, it can be seen that the shark skin generally has the effect of decreasing the size of the reversing flow region as well as the magnitudes of reversing flow within that region. The results at these higher angles of attack show strong evidence that the scales are bristling and impeding the reversal of the low momentum fluid within the boundary layer. While flow separation may still be present, the degree to which the flow separates is altered by the bristling of the scales. When comparing the data at the high angles of attack to the lower angles of attack, it becomes clear that there is a threshold shearing

stress required to bristle the scales. This explains why there is a large difference between the two surfaces at higher angles of attack, where the flow reversal is more prevalent and is stronger. When comparing to the results obtained by Lee and Jang (2005), simply having stationary riblets, which are comparable in size to the scales of the Shortfin Mako, at Reynolds numbers above 40,000 resulted in an increase in the size of the separated region. This suggests that the scales are bristling when encountering reversing and separating flow conditions.

Similar conclusions about the effectiveness of the sharkskin in controlling separation can be drawn from the cylinder results. For all Reynolds numbers, a 10% approximate decrease in the height of the separated region is seen. Once again, the magnitudes of the reversing flow are generally less over the shark skin surface. Contours of the same magnitude of average backflow tend to occur approximately 5% further along the circumference for the case of the shark skin. The drag estimation further supports the hypothesis that the scales are bristling and impeding the flow separation. It was found that there was an average of 18% drag reduction when applying the shark skin to the cylinder. Because flow is separating, the major contribution to drag comes from pressure drag. Such large alteration in the drag over the cylinder must be due to some alteration of the separated flow characteristics over the cylinder. However, further inquiries into drag measurements may reveal a better estimation of the drag differences. These drag measurements do give strong evidence that the flow control is due to the bristling of the scales. When comparing to the results presented by Lee (2005), an increase in drag was found due to the presence of riblets. A decrease in drag suggests that some mechanism other than the scales acting as stationary riblets is responsible for controlling the flow separation.

## 5.2 ECOLOGICAL IMPLICATIONS FOR THE SHORTFIN MAKO

As previously stated, the Shortfin Mako is considered to be one of the fastest swimming sharks. While the Shortfin Mako can be large in size, reaching lengths up to 408 cm, it has many morphological qualities that are conducive to fast agile swimming. One such quality, which is suggested by this research, is the separation control aspect found in the bristling of the scales over the body of the shark. Other qualities include the size and shape of caudal fin which provides the majority of the thrust for a thunniform swimmer (Maia et al., 2012).

Along with the morphological characteristics, the Shortfin Mako also has various muscular adaptations for high speed swimming. One such adaptation is that the Shortfin Mako is an endotherm, meaning the animal can regulate its own body temperature. An elevation in body temperature in certain regions of the body contributes to the increased muscle power needed for high speed motion (Carey et al., 1969). It has also been suggested by Donley et al. (2007) that at higher muscle temperatures between 15-28°C, which are normally experienced by the Shortfin Mako, the optimal cycle frequency for power is greater for the Shortfin Mako than in a comparable ectothermic shark. Such an increase in temperature may be due to the higher metabolic rates found in the Shortfin Mako, which is considered to have among the highest routine and maximum metabolic rates of all shark species (Sepulveda et al., 2007). All of these factors contribute to the speed and agility of the Shortfin Mako.

## 5.3 FUTURE WORK

Several aspects of these experiments can be further investigated to provide more insight into the separation control mechanisms of shark skin. One of which is the shear required to bristle the scales. Because this experiment was run at predetermined Reynolds numbers,

calculation of the minimum shear required to bristle the scales was not possible. Future experiments involving a flat surface with applied shark skin run at incremental Reynolds numbers would give more insight into this matter.

In order to rule out the possibility that the shape and thickness of the skin played a part in the alteration of the flow, further tests may be conducted with the shark skin on the cylinder painted, as what was done for the pectoral fin. If any hydrodynamic benefits were gained from irregularities in the applied sample, they will become evident when comparing to the shark skin surface. Another test to be considered is running the cylinder in the reversed flow direction. If the scales do in fact bristle as is hypothesized, the reversal of the flow over the shark skin samples will have a detrimental effect on the flow characteristics when compared to the smooth cylinder.

While a momentum analysis does give a glimpse into the drag characteristics of the specimen, many errors can arise in this process. In order to fully understand the effects on drag, direct force measurements would need to be made. Currently, there is no means to take force measurements in the water tunnel at the University of Alabama. With this capability, the drag over objects could be directly measured and compared to those with applied shark skin.

## REFERENCES

- Afroz, F. 2014, "Laminar and turbulent boundary layer separation control of mako shark skin", a dissertation, The University of Alabama.
- Andino, M. Y., Braud C., Glauser, M. N., Higuchi, H., and Van Langen, P., "Global Effects of Flow Control over a NACA 4412 Hydrofoil," no. June, pp. 1–12, 2005.
- Bechert, D. W., Bruse, M., Hage, W. & Meyer, R. 2000. Fluid mechanics of biological surfaces and their technological application. *Naturwissenschaften* 80:157-171
- Blake RW. (1983). Fish Locomotion. Cambridge: Cambridge University Press. 208 p.
- Brandner, P.A. and Walker, G.J. 2002. Hydrodynamic performance of a vortex generator. *Experimental Thermal and Fluid Science* 27:573-582
- Bruse, D. W. B. M. and Meyer, W. H. R., "Fluid Mechanics of Biological Surfaces and their Technological Application," pp. 157–171, 2000.
- Bushnell, D. 1983. Turbulent drag reduction for external flows, *AIAA Paper 83-0227*
- Carey, F. G., & Teal, J. M. (1969). Mako and porbeagle: warm-bodied sharks. *Comparative biochemistry and physiology*, 28(1), 199-204.
- Compagno, L. J. (1984). *Sharks Of The World Vol 4 Part 2*, p 109-113.
- Donley, J. M., Shadwick, R. E., Sepulveda, C. A., & Syme, D. A. (2007). Thermal dependence of contractile properties of the aerobic locomotor muscle in the leopard shark and shortfin mako shark. *Journal of Experimental Biology*, 210(7), 1194-1203.
- Horton, H.P. 1968. Laminar Separation Bubbles in Two and Three Dimensional Incompressible Flow. University of London, UK.
- Howard, F. & Goodman, W. 1985. Axisymmetric bluff-body drag reduction through geometrical modification. *J. Aircraft* 22:516-522.
- Land, A., Bradshaw, M., Smith, J., Wheelus, J., Motta, P., Habegger, M. & Hueter, R. 2014. Movable shark scales act as a passive dynamic micro-roughness to control flow separation. Submitted to Bioinspiration and Biomimetics.

- Lang, A. & Hidalgo, P. 2009. Cavity Flow Characterization of the Bristled Shark Skin Microgeometry. AIAA-2009-1107
- Lang, A., Motta, P., Hueter, R. Habegger, M.L. & Afroz, F. 2011. Shark skin separation control mechanisms. *Marine Tech. Soc. J.* 45(4):208-215
- Lin, J. 2002. Review of research on low-profile vortex generators to control boundary-layer separation. *Prog. in Aero. Sci.* 38:389-420
- Lee, S.-J. and Jang, Y.-G. 2005. Control of flow around a NACA 0012 airfoil with a micro-riblet film. *Journal of Fluids and Structures* 20:659-672
- Lee, S., Lim, H., Han, M., & Lee, S.S. 2005. Flow control of circular cylinder with a V-grooved micro-riblet film. *Fluid Dynamics Research* 37:246-266
- Maia, A.M.R., Wilga, C.A.D., & Lauder, G.V. 2004. Biomechanics of Locomotion in Sharks, Rays, and Chimaeras. In: *Biology of Sharks and Their Relatives*, Second Edition, eds. Carrier, J.C, Musick, J.A., & Heithaus, M.R., 125-151. CRC Press.
- Maia, A., Queiroz, N., Correia, J. P., & Cabral, H. (2006). Food habits of the shortfin mako, *Isurus oxyrinchus*, off the southwest coast of Portugal. *Environmental biology of fishes*, 77(2), 157-167.
- Motta, P., Habegger, M.L., Lang, A., Hueter, R., and J. Davis. 2012. Scale morphology and flexibility in the shortfin mako *Isurus oxyrinchus* and the blacktip shark *Carcharhinus limbatus*. *J. Morphology*. 273: 1096-1110.
- Naylor, G., Martin, A., Mattison, E., & Brown, W. 1997. The inter-relationships of lamniform sharks: Testing phylogenetic hypotheses with sequence data. In: *Molecular Systematics of Fishes*, eds. Kocher, T.D., & Stepien, C., 199-217. New York: Academic Press.
- Reif, W.E. 1985a. Morphology and hydrodynamic effects of the scales of fast swimming sharks *Fortschr. Zool.* 30 483-5.
- Schatz, M., Knacke, T., and Thiele, F., Meyer, R., Hage, W., & Bechert, D.W. (2004), Separation control by self-activated moveable flaps, AIAA-2004-1243.
- Schlichting, H. 1979. Boundary-Layer Theory, 7th ed. McGraw-Hill, New York, NY. pp. 555-595
- Schubauer, G.B. 1936. Airflow in a separating boundary layer. *NACA Report No. 527*
- Sepulveda, C.A., Graham, J.B., and Bernal, D. (2007). Aerobic metabolic rates of swimming juvenile mako sharks, *Isurus oxyrinchus*. *Mar. Bio.* 152: 1087-1094.

- Smith, J.A., 2011, "Turbulent separation control effects of mako shark skin samples on a NACA 4412 hydrofoil," a thesis, University of Alabama.
- Stevens, J. 2009. The biology and ecology of the shortfin mako shark, *Isurus oxyrinchus*. In: *Sharks of the Open Ocean: Biology, Fisheries and Conservation*, eds. Camhi, M.D., Pikitch, E.K., Babcock, E.A., 87-94. Oxford, UK: Blackwell Publishing Ltd.
- Tani, I., Low-speed flows involving bubble separation. *Progress in Aerospace Sciences* 5:70-103.
- Videler, J. 1995. Body surface adaptations to boundary-layer dynamics. *Symp. of the Soc. for Exp. Bio.* 49:1-20
- Willert, C.E. & Gharib, 1991. M. Digital image particle velocimetry. *Experiments in Fluids* 10, 181-193.

## APPENDIX- UNCERTAINTY ANALYSIS

Several sources of error and uncertainty are present using the particle image velocimetry techniques described in the experimental configuration section of this paper. One source of error arises in the actual PIV processing itself. A study by Willert and Gharib (1991) found that approximately 1% uncertainty exists in the calculation of particle displacement velocity. This is due to the definition of the location of a particle. Other sources of error may arise when setting up the experiment. In order to have the optimum number of particles in the measurement window, the seeding in the water tunnel must be correct. Too many or too few particles can be detrimental to an experiment. Also, particles that have been sitting in the tunnel for long periods of time may no longer be neutrally buoyant, and therefore, will not correctly follow the path of the flow.

One source of error may be found in the manual calculation of the length scales used for calibration of the PIV processing software. A handheld ruler is placed in the laser field and an image is taken. The length scale is then calculated by measuring the number of pixels in a given length on the ruler. For the data in this experiment, the average length scale was found to be approximately 53  $\mu\text{m}/\text{pix}$ . Assuming that the variation in the location of the ruler markings is approximately 5 pixels, this gives rise to an error of about 1.25% in the calculation of the length scale. Because the height of the camera is not changed between runs, this maximum possible error would be present in all data. Error also lies in the calculation of vectors near the surface of the models tested. Because the surface of the object may be in the middle of a processing grid,

error to where the actual surface lies may arise. Using the grid height of 24 pixels, a max error of 1.75% may be present in the location of the model surface.

Another uncertainty arises in the averaging scheme used to determine the backflow coefficient. When the raw data is processed, some vectors are determined to be 'bad' due to insufficient seeding, particles moving out of the laser sheet, etc. When calculating the backflow coefficient, these bad vectors are ignored. Therefore, the total number of samples that the data was averaged over was less than 4800 for the calculation of the backflow coefficient. When sampling the number of valid vectors calculated, the minimum number of 'good' vectors was found to be approximately 4400. This is a maximum difference of 8.3%. Steps to reduce this error may include reducing 3-dimensional flow over the object as well as ensuring the seeding is sufficient to produce valid vectors within the processing windows.